J. Fluid Mech. (2012), *vol.* 702, *pp.* 157–187. © Cambridge University Press 2012
doi:10.1017/jfm.2012.166

Flotation and free surface flow in a model for subglacial drainage. Part 2. Channel flow

I. J. Hewitt[1]†, C. Schoof[2] and M. A. Werder[3]

[1] Department of Mathematics, University of British Columbia, 1984 Mathematics Road, Vancouver, BC, Canada V6T 1Z2

[2] Department of Earth and Ocean Sciences, University of British Columbia, 6339 Stores Road, Vancouver, BC, Canada V6T 1Z4

[3] Department of Earth Sciences, Simon Fraser University, 8888 University Drive, Burnaby, BC, Canada V5A 1S6

(Received 22 June 2011; revised 31 January 2012; accepted 30 March 2012; first published online 23 May 2012)

We present a new model of subglacial drainage incorporating flow in a network of channels and a porous sheet, with water exchange between the two determined by pressure gradients. The sheet represents the average effect of many linked cavities, whilst the channels emerge from individual cavities that enlarge due to dissipation-induced melting. The model distinguishes cases when the water pressure drops to zero, in which case it allows for the drainage space to be only partially filled with water (free surface flow), and when the pressure reaches the ice overburden pressure, in which case it allows for uplift of the ice to whatever extent is needed to accommodate the water (flotation). Numerical solutions are found for a one-dimensional flow-line version of the model. The results capture typically observed or inferred features of subglacial drainage systems, including open channel flow at the ice margin, seasonal channel evolution, and high water pressures and uplift of the ice surface driven by rapid changes in water supply.

Key words: ice sheets, hydrology, variational methods

1. Introduction

Glaciers and ice sheets move through a combination of internal deformation and sliding at the bed. Significant sliding can occur whenever water is present, since it allows slip at the interface between ice and bed. Water may be produced from melting at the bed, due to a combination of geothermal and frictional heating; often, however, there is a much larger supply that comes from melting on the ice surface, descending to the bed through crevasses and moulins. This supply can vary on diurnal, annual and decadal time scales, and is known to cause significant spatial and temporal variations in the velocity of mountain glaciers (e.g. Hooke, Brzozowski & Bronge 1983; Kamb *et al.* 1985; Iken & Bindschadler 1986; Willis 1995; Raymond *et al.* 1995; Jansson 1996). Recent observations from Greenland have shown that large sections of the ice there also undergo rapid acceleration and deceleration, which has been attributed, at least partly, to changing meltwater conditions at the bed (Zwally *et al.* 2002; Joughin

† Email address for correspondence: hewitt@math.ubc.ca

https://doi.org/10.1017/jfm.2012.166 Published online by Cambridge University Press

et al. 2008; Van de Wal *et al.* 2008; Shepherd *et al.* 2009; Bartholomew *et al.* 2010). It is still not clear, however, what the long-term effect of these changes is for the mass balance of the ice sheet and for consequent sea level rise. Ice flow models that are coupled to models of the drainage system and its effect on sliding are ultimately required in order to assess this.

One of the most important observations is that a greater quantity of meltwater does not necessarily correlate with increased sliding. This is believed to be due to the ongoing evolution of the subglacial drainage system which may, at different times, be more, or less, able to accommodate large quantities of water. Theoretical models and field evidence both suggest that it is the effective pressure at the bed, defined as the normal stress in the ice minus the water pressure, that plays a key role in controlling the rate of sliding (Budd, Keage & Blundy 1979; Bindschadler 1983; Iken & Bindschadler 1986; Fowler 1986; Schoof 2005). Lower effective pressure generally allows for faster sliding, either by weakening underlying till which can then deform more readily, or by reducing the contact area between ice and bedrock and therefore lessening the drag. The main goal for our model is therefore to predict the effective pressure.

The conventional description of subglacial drainage, which motivates our model, makes a broad distinction between 'distributed' and 'channelized' water flow (Fountain & Walder 1998). In a distributed system, water is spread out over the bed in what can effectively be described as a porous drainage layer (Flowers & Clarke 2002; Creyts & Schoof 2009; Hewitt 2011). For the purpose of constructing our model we envisage it as a series of linked cavities, which form when the ice slides over asperities in the bed (Lliboutry 1969; Walder 1986; Fowler 1987; Kamb 1987); very similar behaviour can however be expected if the water flows through porous till or a network of 'canals' (Walder & Fowler 1994), and the model may apply with minimal modification to both hard and soft bedded glaciers. In a channelized system the water collects into a few distinct channels, incised upwards into the ice (Shreve 1972; Röthlisberger 1972; Nye 1976; Spring & Hutter 1982; Schoof 2010). The water flowing within these channels dissipates energy, which acts to melt the surrounding ice and maintain them open against inward creep (the basal water pressure is generally lower than the ice pressure, so viscous deformation of the ice acts to close down the drainage space).

In general, a distributed system is expected when meltwater discharge is low, whereas channels are expected when it is high. In places where surface meltwater penetrates to the bed, the discharge can vary enormously over the course of a year and the structure of the drainage system consequently evolves (Hock & Hooke 1993; Raymond *et al.* 1995; Gordon *et al.* 1998; Nienow, Sharp & Willis 1998; Copland, Sharp & Nienow 2003). During the winter, when discharge is low, water occupies the slow distributed system, and channels created during the preceding summer tend to close down. In spring, meltwater from the surface finds its way to the bed; the distributed system is unable to cope with this sudden influx and high water pressures ensue. The larger discharge also enables channels to form, however, which eventually causes the water pressure to drop. The response to subsequent variations in the melting rate depends upon their magnitude and rapidity: slower and smaller changes may be accommodated by the channels with minimal impact on the water pressure, whereas sudden or large changes may again result in elevated pressures.

Whilst this description is highly idealized and the specifics are often different, it gives some idea of the general behaviour we hope to model. In particular, we note that the pressure can undergo large fluctuations as a result of the varying meltwater supply. In this and a companion paper (Schoof, Hewitt & Werder 2012), we particularly focus

https://doi.org/10.1017/jfm.2012.166 Published online by Cambridge University Press

on what happens when the water pressure exceeds the overburden ice pressure (i.e. the effective pressure becomes negative) or reaches zero. In the first case, which we refer to as 'overpressure', rapid uplift and widespread separation between ice and bed is expected. In the second, 'underpressure', an air or vapour pocket should form and the drainage system becomes only partially filled with water. Most current models do not take account of these effects and would unphysically predict negative effective pressure or water pressure (there are some exceptions: Tsai & Rice (2010), for instance, present a hydrofracture model for high water pressure lake drainage, and Schuler & Fischer (2009) account for partially filled channels).

In the companion paper (Schoof *et al.* 2012) we presented a simple 'sheet' model for a distributed drainage system, in which the water pressure is constrained so that it always lies between zero and the overburden pressure. When either of these bounds are reached, the 'normal' model is modified to allow for the sheet to be only partially filled, or for additional uplift to occur. The purpose of the present paper is to extend those ideas to a model that includes channelized drainage. In the process, we demonstrate how existing continuum models of distributed drainage can be coupled to an arbitrary network of channels.

In § 2 we describe how the sheet model outlined in Schoof *et al.* (2012) can be combined with a network of channels. Section 3 then explains how this extended model is modified when the water pressure reduces to zero or reaches overburden. We also show how a variational principle can be used to determine the regions on which the pressure reaches these bounds, and outline the numerical procedure we have used to solve the model in one spatial dimension. In one dimension the combined sheet-channel model resembles other flow-line 'dual-permeability' models (e.g. Flowers *et al.* 2004; Hewitt & Fowler 2008; Pimentel & Flowers 2010), and is able to capture many aspects of the drainage system behaviour that are inferred from observations. Section 4 presents a number or illustrative results, and in § 5 we discuss some of the implications and limitations of this model. Readers less interested in the mathematical details may wish to gloss over § 3 and go straight to the solutions in § 4.

2. A sheet-channel model for subglacial drainage

We begin in this section with the 'normal' pressure regime, assuming that the drainage system is water filled and that the water pressure, p_w, lies between atmospheric and overburden pressures. Then, in § 3, we discuss the modifications required when p_w passes outside this range. The effective pressure is defined by

$$N = p_i - p_w, \tag{2.1}$$

and the ice pressure is assumed to be cryostatic, $p_i = \rho_i g H$, where ρ_i is the ice density, g the gravitational acceleration and $H = H(x, y)$ the ice thickness. (For simplicity we assume that p_i is cryostatic throughout this paper; if there are significant deviatoric stresses we should instead define the effective pressure in (2.1) as $-\sigma_n - p_w$, where $-\sigma_n$ is the average normal stress at the bed, and all references to p_i or to 'overburden' should be interpreted as $-\sigma_n$. The normal stress is usually well-approximated by $\rho_i g H$, even when the pressure itself is not cryostatic.)

2.1. *Sheet dynamics*

In Schoof *et al.* (2012) we described a distributed linked-cavity drainage system as a porous 'sheet', represented by an average water depth $h_w(x, y, t)$ occupying the average drainage system depth $h(x, y, t)$ (in the normal pressure regime, water fills all of the

https://doi.org/10.1017/jfm.2012.166 Published online by Cambridge University Press

cavities and $h_w = h$, but we maintain the distinction for use in the next section). Since cavities open through sliding of the ice over bedrock bumps, and close due to inward creep of the ice roof (Walder 1986; Kamb 1987), the depth h is assumed to evolve according to

$$\frac{\partial h}{\partial t} = v_o(h) - v_c(N, h), \quad v_o(h) = u_b(h_r - h)/l_r, \quad v_c(N, h) = \tilde{A} h |N|^{n-1} N, \tag{2.2}$$

where these specific forms for v_o and v_c are chosen as parameterizations of the opening and closing processes, u_b is the sliding speed (assumed known for this paper), h_r is a typical height of bedrock bump and l_r is the typical spacing of such bumps, $\tilde{A}$ is the rheological constant for the ice times an order one geometrical factor that depends on the shape of the cavities, and n is the exponent in Glen's law. Note that according to (2.2) it is impossible for the sheet depth to exceed h_r unless the effective pressure becomes negative; physically, this is because cavities cannot become arbitrarily large but are limited by the size of the bedrock bumps.

Water flow through the porous sheet is described by

$$\boldsymbol{q} = -k h_w^{\alpha} |\nabla \phi|^{\beta - 2} \nabla \phi, \tag{2.3}$$

where k is a permeability constant, $\alpha > 1$ and $\beta > 1$ are model parameters for the water flow (taken to be $\alpha = 5/4$ and $\beta = 3/2$, motivated by a Darcy–Weisbach law), and ϕ is the hydraulic potential. Mass conservation in the sheet is then expressed as

$$\frac{\partial h_w}{\partial t} + \nabla \cdot \boldsymbol{q} = m, \tag{2.4}$$

where $m = m(x, y, t)$ is the meltwater source. In general, m has contributions from both basal melting and from surface run-off through crevasses and moulins. In this paper it is simply prescribed, but it should ideally be determined by coupling to models for surface mass balance, englacial water routing and heat transport in the ice.

The hydraulic potential ϕ is given by

$$\phi = \rho_w g b + \rho_w g h_w + p_w, \tag{2.5}$$

where ρ_w is the water density and $b = b(x, y)$ is the bed elevation. We also define

$$\phi_0(x, y) = \rho_i g H(x, y) + \rho_w g b(x, y) \quad \text{and} \quad \phi_m(x, y) = \rho_w g b(x, y), \tag{2.6}$$

as the potentials corresponding to the ice surface and the bed elevation (see figure 1), taken to be steady on the time scales of interest here. The effective pressure can then be written in terms of ϕ as

$$N = \phi_0 + \rho_w g h_w - \phi. \tag{2.7}$$

By including the term $\rho_w g h_w$, we attempt to account for the hydrostatic pressure variation within the water layer, and are therefore taking p_w to be the water pressure at the top of the sheet (as in the definition of effective pressure (2.1)). Most models, including our sheet model in Schoof *et al.* (2012), ignore this pressure variation since it is typically very small, but it may be important in allowing for subglacial lakes to form when the hydraulic potential would otherwise have a local minimum.

As discussed by many previous authors (e.g. Walder 1986; Kamb 1987; Schoof 2010; Hewitt 2011), individual cavities have the potential to grow more rapidly than suggested by v_o in (2.2) if the heat generated by water flow through them causes significant melting of the ice roof. This leads to the idea that 'cavities' can turn into 'channels', the distinction being that channels are maintained open through the

https://doi.org/10.1017/jfm.2012.166 Published online by Cambridge University Press

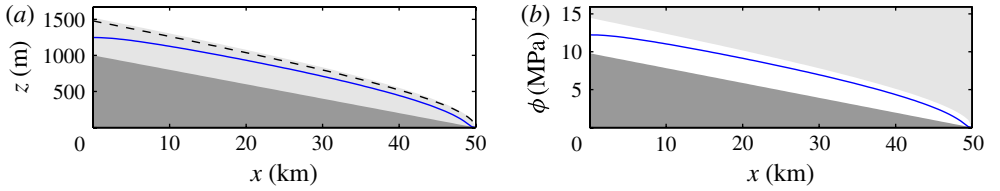


FIGURE 1. (Colour online available at journals.cambridge.org/flm) (*a*) An example glacier profile showing: bed elevation $z = b(x)$ (dark shading), surface elevation $z = b(x) + H(x)$ (lighter shading), the flotation level for water (dashed) and typical hydraulic head for basal water (solid). (*b*) The equivalent profile of hydraulic potential, with the boundaries of the shaded regions representing the hydraulic potentials, $\phi_m(x)$ and $\phi_0(x)$, that correspond to the bed and the flotation level (see (2.6)).

balance of ice melting and creep closure, without any requirement for the sliding term. Including the heating effect in (2.2) results in an ill-posed model, however, since it can lead to unbounded growth of h in an infinitesimally narrow region. This physical process of channelization is nevertheless one we would like to describe in the model, and we propose a method to do so below. Essentially we allow a certain collection of the individual cavities to turn into channels, and these are modelled separately, as line sinks to the two-dimensional sheet.

2.2. *Channel dynamics*

In the simplest theory for subglacial channels (Röthlisberger 1972; Nye 1976), the channel cross-sectional area, S, evolves according to melting and creep closure:

$$\frac{\partial S}{\partial t} = \frac{\Xi}{\rho_i L} - v_{cC}(N, S), \qquad v_{cC}(N, S) = \hat{A} S |N|^{n-1} N, \tag{2.8}$$

where $\hat{A}$ is a rheological constant (potentially different from $\tilde{A}$ due to the different geometries of channels and cavities), L is the latent heat of fusion and Ξ is the heat generated by water flow in the channel. This assumes that all heat generated is instantly transferred to the ice walls and results in melting. If a turbulent flow law such as

$$Q = -k_C S_w^{\alpha} \left| \frac{\partial \phi}{\partial s} \right|^{\beta-2} \frac{\partial \phi}{\partial s}, \tag{2.9}$$

is used to describe the discharge Q through the channel, the heat dissipated is $|Q \partial\phi/\partial s|$. In (2.9), k_C is a constant related to the friction law and geometry assumed for the channel, $\alpha = 5/4$ and $\beta = 3/2$ are again related to the turbulent flow parameterization and s denotes horizontal distance along the channel. Note that we again distinguish the water-filled cross-sectional area, S_w, from the total cross-sectional area, S, for later use; in the normal pressure regime, we always have $S_w = S$.

In order to marry this description of a channel with the cavities that make up the sheet, we suppose that S denotes the cross-sectional area of a channel that lies 'above' the sheet depth h (see figure 2). We envisage, however, that the channel initially evolves out of one of the individual cavities that make up the sheet (Walder 1986; Kamb 1987). The heat production that goes into melting the channel therefore includes both that due to water flow within the channel area, (2.9), and that due to the water flow in the original cavity. The latter can be approximated by $l_r k h_w^{\alpha} |\partial\phi/\partial s|^{\beta}$, taking l_r

https://doi.org/10.1017/jfm.2012.166 Published online by Cambridge University Press

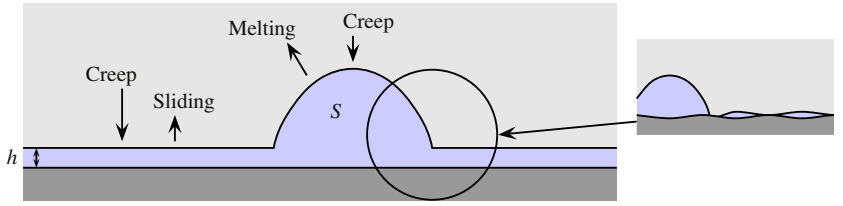


FIGURE 2. (Colour online) Schematic representation of a water-filled channel and sheet (the depth of the sheet is exaggerated and is not really a continuous sheet; it comprises small connected cavities as shown on the right). The sheet has average depth h, typically controlled by sliding over bedrock bumps and creep closure due to a positive effective pressure. The channel has cross-sectional area S, controlled by melting due to turbulent dissipation of the water flowing within it and creep closure due to a positive effective pressure.

to be the typical cavity width, and $kh_w^\alpha|\partial\phi/\partial s|^\beta$ the heat generated per unit width in the sheet. Thus, the dissipation in (2.8) is taken to be

$$\Xi = k_C S_w^\alpha \left|\frac{\partial\phi}{\partial s}\right|^\beta + l_r k h_w^\alpha \left|\frac{\partial\phi}{\partial s}\right|^\beta. \tag{2.10}$$

In effect, this defines S to be the drainage space created by melting of one of the cavity roofs. When there is little water flow this area is very small compared with the cavity size, the first term in (2.10) is negligible compared with the second, and S is small. As the discharge is increased, however, S increases, and at some stage the first term in (2.10) dominates the second term; this corresponds to the cavity turning into a channel.

The equations describing a channel are completed with a mass conservation equation:

$$\frac{\partial S_w}{\partial t} + \frac{\partial Q}{\partial s} = \frac{\Xi}{\rho_w L} + \kappa, \tag{2.11}$$

in which κ is the water source from the surrounding sheet, discussed again below. It is straightforward to include additional source terms directly into a channel (if a subglacial channel is fed directly from a moulin, for example) but for this paper we intend to avoid specifics of the *en*glacial hydrologic system and assume all water is fed initially into the sheet, through m.

2.3. *Network approach*

The location and orientation of channels is not known until they form, and in principle we would like to allow them to form anywhere and with any orientation. One way to approximately allow for this, following the network model of Schoof (2010), is to explicitly model the dynamics of individual 'conduits' that can choose to behave as 'cavities' or 'channels'. Channels are inherently localized, however, and if neighbouring conduits all turn into channels they quickly compete with one another for water, all but one reverting to behave as cavities. This observation that most conduits remain as cavities is the motivation for introducing the average sheet description of cavities, since it allows us to account for many more of them than can feasibly be included in a discrete formulation.

For the current model we therefore propose to allow for a network of 'potential' channels, each described by (2.8), overlying the porous sheet. In effect, we single

https://doi.org/10.1017/jfm.2012.166 Published online by Cambridge University Press

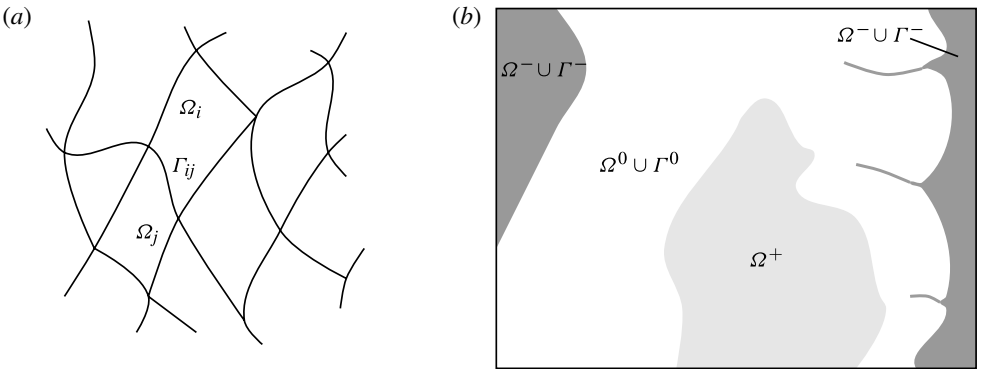


FIGURE 3. (*a*) A channel network, with channel segments labelled Γ_{ij} divides the sheet domain into distinct regions Ω_i. (*b*) A schematic plan view of the bed showing example domains of overpressure and underpressure (see (3.4)–(3.5)). The ice flow is predominantly from left to right.

out certain individual cavities that we allow to turn into channels, on the assumption that the other cavities making up the sheet would in any case remain cavities. Each of the potential channels is free to evolve according to (2.8), and only those with sufficient water flow through them will evolve into channels of any significant size. By including a sufficiently dense network of potential channel segments we hope to allow the evolving network to select its own structure, including, for instance, the merging and splitting of channels.

To be more specific, we suppose that the whole subglacial domain, labelled Ω, is dissected by a network of potential channel segments, Γ, treated as being infinitely thin (figure 3*a*). This divides the sheet domain into many subdomains Ω_i, and the individual channel segments can be labelled Γ_{ij} according to the indices i and j of the subdomains on either side. The porous sheet, described by (2.2)–(2.4), is defined on each Ω_i, and individual channels, described by (2.8)–(2.11), are defined on each Γ_{ij}. With this setup, the source terms to each channel, $\kappa = \kappa_{ij}$, can be written explicitly as

$$\kappa = [\boldsymbol{q} \cdot \boldsymbol{n}]^+_- \equiv \boldsymbol{q}_i \cdot \boldsymbol{n}_i + \boldsymbol{q}_j \cdot \boldsymbol{n}_j, \tag{2.12}$$

where $\boldsymbol{n}_i$ is the normal to the channel pointing outward from Ω_i. The channel segments can therefore be seen as line sources or sinks, providing jump conditions for the sheet flux across them (Hewitt 2011). At nodes of the network where the channels meet, mass conservation requires that the fluxes into and out of the node sum to zero. We also assume that water pressure is continuous between sheet and channel segments, so

$$\phi|_{\Gamma_{ij}} = \phi|_{\partial\Omega_i} = \phi|_{\partial\Omega_j}. \tag{2.13}$$

Boundary conditions are required at the external boundaries $\partial\Omega$; we assume these are either conditions on ϕ (at the ice margin we expect to prescribe that the pressure is atmospheric), or conditions on the fluxes, $q_N = -\boldsymbol{q} \cdot \boldsymbol{n}$, normal to the boundary ($\boldsymbol{n}$ here is the outward normal to the boundary $\partial\Omega$), and label the regions on which these are prescribed as $\partial\Omega_D$ and $\partial\Omega_N$, respectively. Where channels intersect the inflow boundary $\partial\Omega_N$, $Q = Q_N$ is prescribed.

In summary, the model of this section consists of two ordinary differential equations (2.2) and (2.8) for the evolution of sheet depth h and channel area S.

https://doi.org/10.1017/jfm.2012.166 Published online by Cambridge University Press

With $h_w = h$ and $S_w = S$, the combination of these evolution equations with the conservation (2.4) and (2.11), and jump conditions (2.12), yields

$$-\nabla \cdot [kh^\alpha |\nabla\phi|^{\beta-2}\nabla\phi] + v_o(h) - v_c(N,h) - m = 0, \tag{2.14}$$

on each Ω_i, and

$$-\frac{\partial}{\partial s}\left[k_C S^\alpha \left|\frac{\partial\phi}{\partial s}\right|^{\beta-2}\frac{\partial\phi}{\partial s}\right] + \frac{\Delta\rho}{\rho_w}\frac{\Xi}{\rho_i L} - v_{cC}(N,S) + [kh^\alpha|\nabla\phi|^{\beta-2}\nabla\phi\cdot\boldsymbol{n}]_-^+ = 0, \tag{2.15}$$

on each Γ_{ij}, where $\Delta\rho = \rho_w - \rho_i$ is the density difference between water and ice. Together with the expression for N in (2.7) and the prescribed boundary conditions on $\partial\Omega$, these constitute an elliptic problem for the potential ϕ.

3. Overpressure and underpressure

We now describe how the model changes when the water pressure reaches overburden or reduces to zero. The general principle is to assume that the water pressure cannot pass beyond these two bounds; instead, modifications are made to the model when they are reached. In the next subsection we express these pressure bounds as constraints on the hydraulic potential. Then in § 3.2 we discuss how the evolution and transport equations (2.2), (2.4), (2.8) and (2.11) apply to the bounding cases of underpressure and overpressure. In § 3.3 we show how the combination of the equations allows for the hydraulic potential to be determined by a variational formulation.

3.1. *Bounds on the hydraulic potential*

From (2.5) and (2.6), the extreme case $p_w = p_i$ is equivalent to $\phi = \phi_0 + \rho_w g h_w$ and $p_w = 0$ is equivalent to $\phi = \phi_m + \rho_w g h_w$. In fact, p_w was defined as the pressure at the top of the water sheet; in the channels, the zero water pressure bound should more sensibly be applied to the pressure at the top of the channel instead, which is smaller by the hydrostatic factor $\rho_w g \mathscr{H}_w$, where $\mathscr{H}_w$ is the water depth in the channel above the sheet. Given an assumed geometry of the channel, and allowing for it to be only partially filled, $\mathscr{H}_w$ depends on S_w and S, and we write $\mathscr{H}_w(S_w, S)$ (e.g. see appendix B for semicircular channels). If we then define the hydrostatic potentials,

$$\phi_h(x,y,t) = \rho_w g h_w, \quad \phi_{\mathscr{H}}(x,y,t) = \begin{cases} 0 & (x,y) \in \bigcup \Omega_i, \\ \rho_w g \mathscr{H}_w(S_w, S) & (x,y) \in \Gamma, \end{cases} \tag{3.1}$$

and use these to define

$$\left.\begin{aligned} \hat{\phi}_m(x,y,t) &= \phi_m(x,y) + \phi_h(x,y,t) + \phi_{\mathscr{H}}(x,y,t), \\ \hat{\phi}_0(x,y,t) &= \phi_0(x,y) + \phi_h(x,y,t), \end{aligned}\right\} \tag{3.2}$$

then the potential ϕ must always be constrained so that

$$\hat{\phi}_m \leqslant \phi \leqslant \hat{\phi}_0. \tag{3.3}$$

As pointed out earlier, the ϕ_h and $\phi_{\mathscr{H}}$ terms are usually very small, and in Schoof *et al.* (2012) we ignored them (in which case $\hat{\phi}_m = \phi_m$, $\hat{\phi}_0 = \phi_0$). Here we retain them because they turn out to prevent some otherwise singular behaviour.

https://doi.org/10.1017/jfm.2012.166 Published online by Cambridge University Press

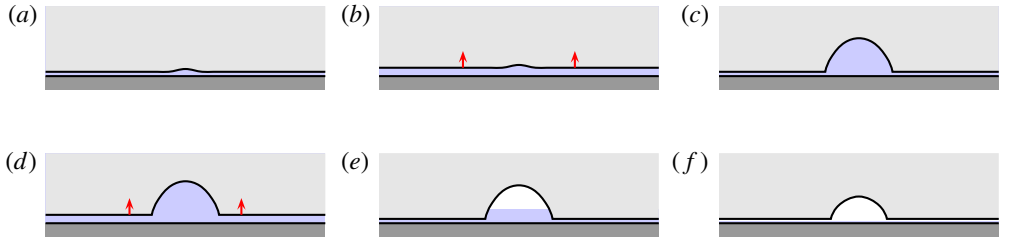


FIGURE 4. (Colour online) Schematic representation of sheet and one channel, with the predominant flow direction out of the page, under different possible flow conditions. (*a*) Low meltwater input: insignificant melting in the channel, essentially all flow is in the sheet; (*b*) increased input: pressure reaches overburden and lifts up the ice, the channel has not had time to develop; (*c*) larger steady input: the channel has grown and draws in water from the sheet; (*d*) increased input: pressure reaches overburden and lifts up the ice, leaving the channel unaltered; (*e*) lower input: pressure falls to a minimum and the channel becomes partially empty; (*f*) still lower input: water level drops enough so that the sheet also becomes partially filled.

At any given time t, we can define the domains on which $\phi = \hat{\phi}_m$ ('underpressure'), and $\phi = \hat{\phi}_0$ ('overpressure'), respectively:

$$\Omega^-(t) = \left\{(x,y) \in \bigcup \Omega_i : \phi = \hat{\phi}_m\right\}, \quad \Gamma^-(t) = \{(x,y) \in \Gamma : \phi = \hat{\phi}_m\}, \tag{3.4}$$

$$\Omega^+(t) = \left\{(x,y) \in \bigcup \Omega_i : \phi = \hat{\phi}_0\right\}, \quad \Gamma^+(t) = \{(x,y) \in \Gamma : \phi = \hat{\phi}_0\}. \tag{3.5}$$

These domains are not known *a priori*, however, and must be determined as part of the solution, as will be shown in § 3.3. First we discuss how the equations are modified on these regions.

3.2. *Evolution and transport equations*

Normal pressure, $\hat{\phi}_m < \phi < \hat{\phi}_0$

When $\hat{\phi}_m < \phi < \hat{\phi}_0$ the model is as described in § 2, with $h = h_w$ and $S = S_w$.

Underpressure, $\phi = \hat{\phi}_m$

When water pressure reaches zero the drainage space becomes only partially filled (see figure 4*e*,*f*). In that case we can have $h_w < h$, and with $\phi = \hat{\phi}_m$, equations (2.2) and (2.4) provide two separate equations for the evolution of h and h_w. Similarly, when $S_w < S$, equations (2.8) and (2.11) provide two separate equations for S and S_w.

In the limiting case when the sheet is just on the verge of becoming partially empty, $h_w = h$, the evolution equations must satisfy the inequality constraint

$$\phi = \hat{\phi}_m, \quad \frac{\partial h_w}{\partial t} \leqslant \frac{\partial h}{\partial t}, \tag{3.6}$$

the two derivatives still being given by (2.4) and (2.2), respectively. Similarly if the channel is on the verge of being partially empty, $S_w = S$, and

$$\phi = \hat{\phi}_m, \quad \frac{\partial S_w}{\partial t} \leqslant \frac{\partial S}{\partial t}. \tag{3.7}$$

With $\phi = \hat{\phi}_m$, the mass equations (2.4) and (2.11) for h_w and S_w are nonlinear diffusion equations, and the continuity of ϕ ensures that h_w and $\mathscr{H}_w(S_w, S)$ must be

https://doi.org/10.1017/jfm.2012.166 Published online by Cambridge University Press

continuous. Note also that the continuity of ϕ implies that the sheet adjacent to a channel cannot reach underpressure until the channel is completely empty (so $S_w = 0$ and $\mathscr{H}_w = 0$). In that case, the channel equation (2.11) serves to determine κ, which provides the jump conditions (2.12) required when solving the sheet equation (2.4). When the channel is still partially filled on the other hand, so $h_w = h$ there, the sheet equations (2.2) and (2.4) together determine the source term κ from (2.12) to use in (2.11).

Overpressure, $\phi = \hat{\phi}_0$

When overburden is reached we assume that widespread uplift of the ice can occur, and that the excess pressure required to cause this is insignificant. The opening equation for the sheet (2.2) no longer holds in this case and instead we allow h to evolve together with h_w according to the mass equation (2.4). This allows for the possibility that h can exceed the roughness level h_r in (2.2), corresponding to complete separation between ice and bed. If the ice is still in contact, however (i.e. $h < h_r$), the rate of separation must be at least as large as that due to the sliding term in (2.2), giving rise to the inequality constraint

$$\phi = \hat{\phi}_0, \quad \frac{\partial h}{\partial t} = \frac{\partial h_w}{\partial t} \geqslant v_o(h) - v_c(N, h), \tag{3.8}$$

(the closure term here is zero since $N = 0$, but it is retained for convenience below). The channel area S, being incised into the ice roof, is unaffected by any uplift of the ice and therefore continues to evolve according to (2.8). With $\phi = \hat{\phi}_0$ known, however, the channel equations (2.8) and (2.11) combine to determine both the evolution of $S = S_w$ and also the source term κ. This determines the jump conditions (2.12) to apply when solving the diffusion equation (2.4) for h_w and h.

3.3. *Variational formulation for hydraulic potential*

To facilitate determining the hydraulic potential we first note that, given current values of h, h_w, S and S_w, we can immediately identify the regions of partially filled cavities and channels as

$$\left.\begin{aligned} \Omega^e &= \left\{(x, y) \in \bigcup \Omega_i : h_w(x, y, t) < h(x, y, t)\right\}, \\ \Gamma^e &= \{(x, y) \in \Gamma : S_w(x, y, t) < S(x, y, t)\}. \end{aligned}\right\} \tag{3.9}$$

Similarly, regions where there is complete separation between ice and bed, are

$$\Omega^f = \left\{(x, y) \in \bigcup \Omega_i : h(x, y, t) > h_r(x, y)\right\}, \quad \Gamma^f = \Gamma \cap \overline{\Omega^f(t)}, \tag{3.10}$$

where $\overline{\Omega^f}$ denotes the closure of Ω^f.

On $\Omega^e \cup \Gamma^e$, we know immediately that $\phi = \hat{\phi}_m$, and on $\Omega^f \cup \Gamma^f$, we must have $\phi = \hat{\phi}_0$ (since $h > h_r$ is only possible if ϕ reaches $\hat{\phi}_0$). The remainder of the domain is labelled by

$$\Omega^c = \bigcup \Omega_i \setminus (\Omega^e \cup \Omega^f), \quad \Gamma^c = \Gamma \setminus (\Gamma^e \cup \Gamma^f), \tag{3.11}$$

and it is this region on which the potential must be solved for, subject to $\hat{\phi}_m \leqslant \phi \leqslant \hat{\phi}_0$. On these subdomains we have $h_w = h < h_r$ and $S_w = S$. The following variational formulation echoes that in Schoof *et al.* (2012), to which the reader is referred for further details.

https://doi.org/10.1017/jfm.2012.166 Published online by Cambridge University Press

Considering the various possibilities explained in § 3.2, on Ω^c we must either have $\hat{\phi}_m < \phi < \hat{\phi}_0$, in which case $\partial h_w/\partial t = \partial h/\partial t$ as in (2.14), or we have one of the bounding inequalities (3.6) and (3.8). Thus, one of the following three cases applies on Ω^c:

$$\hat{\phi}_m < \phi < \hat{\phi}_0 \quad \text{and} \quad -\boldsymbol{\nabla}\cdot[kh^\alpha|\boldsymbol{\nabla}\phi|^{\beta-2}\boldsymbol{\nabla}\phi] + v_o(h) - v_c(N,h) - m = 0, \tag{3.12a}$$

$$\phi = \hat{\phi}_0 \quad \text{and} \quad -\boldsymbol{\nabla}\cdot[kh^\alpha|\boldsymbol{\nabla}\phi|^{\beta-2}\boldsymbol{\nabla}\phi] + v_o(h) - v_c(N,h) - m \leqslant 0, \tag{3.12b}$$

$$\phi = \hat{\phi}_m \quad \text{and} \quad -\boldsymbol{\nabla}\cdot[kh^\alpha|\boldsymbol{\nabla}\phi|^{\beta-2}\boldsymbol{\nabla}\phi] + v_o(h) - v_c(N,h) - m \geqslant 0. \tag{3.12c}$$

Similarly it is evident from § 3.2 that the channel equations (2.8) and (2.11) always hold on Γ^c with $\partial S/\partial t = \partial S_w/\partial t$, except for the momentary case in (3.7) when the channel is on the verge of becoming partially empty. One of the following two cases must therefore apply on Γ^c:

$$\hat{\phi}_m < \phi \leqslant \hat{\phi}_0 \quad \text{and} \quad -\frac{\partial}{\partial s}\left[k_C S^\alpha \left|\frac{\partial\phi}{\partial s}\right|^{\beta-2}\frac{\partial\phi}{\partial s}\right] + \frac{\Delta\rho}{\rho_w}\frac{\Xi}{\rho_i L} - v_{cC}(N,S) - \kappa = 0, \tag{3.13a}$$

$$\phi = \hat{\phi}_m \quad \text{and} \quad -\frac{\partial}{\partial s}\left[k_C S^\alpha \left|\frac{\partial\phi}{\partial s}\right|^{\beta-2}\frac{\partial\phi}{\partial s}\right] + \frac{\Delta\rho}{\rho_w}\frac{\Xi}{\rho_i L} - v_{cC}(N,S) - \kappa \geqslant 0. \tag{3.13b}$$

The variational form is obtained by multiplying (3.12) and (3.13) by $(\theta - \phi)$, where θ is a test function, satisfying $\hat{\phi}_m \leqslant \theta \leqslant \hat{\phi}_0$. Then integrating by parts over each sheet segment Ω_i^c (that is, $\Omega^c \cap \Omega_i$) and channel segment Γ_{ij}^c (that is, $\Gamma^c \cap \Gamma_{ij}$), and considering all of the different cases in (3.12) and (3.13), we find

$$\int_{\Omega_i^c} kh^\alpha|\boldsymbol{\nabla}\phi|^{\beta-2}\boldsymbol{\nabla}\phi\cdot\boldsymbol{\nabla}(\theta-\phi) - v_c(\hat{\phi}_0-\phi,h)(\theta-\phi) - [m - v_o(h)](\theta-\phi)\,\mathrm{d}\Omega + \int_{\partial\Omega_i^c}\boldsymbol{q}\cdot\boldsymbol{n}(\theta-\phi)\,\mathrm{d}\Gamma \geqslant 0, \tag{3.14}$$

for each Ω_i^c, and

$$\int_{\Gamma_{ij}^c} k_C S^\alpha\left|\frac{\partial\phi}{\partial s}\right|^{\beta-2}\frac{\partial\phi}{\partial s}\frac{\partial(\theta-\phi)}{\partial s} - v_{cC}(\hat{\phi}_0-\phi,S)(\theta-\phi) - \kappa(\theta-\phi) + \frac{\Delta\rho}{\rho_w}\frac{\Xi}{\rho_i L}(\theta-\phi)\,\mathrm{d}\Gamma + [Q(\theta-\phi)]_{\partial\Gamma_{ij}^c} \geqslant 0, \tag{3.15}$$

for each Γ_{ij}^c. The final boundary terms are evaluated at each end of Γ_{ij}^c. We then sum together all of these inequalities, assuming that θ satisfies the same Dirichlet conditions as ϕ on all points of $\partial\Omega^c$ and $\partial\Gamma^c$ interior to Ω and on the outer boundary $\partial\Omega_D$. Remembering the definition of κ in (2.12), and the conservation of mass at the network nodes, most of the boundary terms cancel out or disappear, and we are left with

$$\int_{\Omega^c} kh^\alpha|\boldsymbol{\nabla}\phi|^{\beta-2}\boldsymbol{\nabla}\phi\cdot\boldsymbol{\nabla}(\theta-\phi) - v_c(\hat{\phi}_0-\phi,h)(\theta-\phi) - [m-v_o(h)](\theta-\phi)\,\mathrm{d}\Omega + \int_{\Gamma^c} k_C S^\alpha\left|\frac{\partial\phi}{\partial s}\right|^{\beta-2}\frac{\partial\phi}{\partial s}\frac{\partial(\theta-\phi)}{\partial s} - v_{cC}(\hat{\phi}_0-\phi,S)(\theta-\phi)\,\mathrm{d}\Gamma$$

https://doi.org/10.1017/jfm.2012.166 Published online by Cambridge University Press

$$- \int_{\partial\Omega^c\cap\partial\Omega_N} q_N(\theta-\phi)\,\mathrm{d}\Gamma - Q_N(\theta-\phi)|_{\partial\Gamma^c\cap\partial\Omega_N}$$
$$+ \int_{\Gamma^c} \frac{\Delta\rho}{\rho_w}\frac{\Xi}{\rho_i L}(\theta-\phi)\,\mathrm{d}\Gamma \geqslant 0, \tag{3.16}$$

for all suitable test functions θ. We have written $\int_{\Omega^c} = \sum_i \int_{\Omega_i^c}$, $\int_{\Gamma^c} = \sum_{i,j}\int_{\Gamma_{ij}^c}$. The two remaining boundary terms on the penultimate line come from locations where $\Omega^c \cup \Gamma^c$ intersects the inflow boundary $\partial\Omega_N$.

The final term represents the dissipation in the channel, and is written separately because it requires special attention. We would like to convert the inequality (3.16) into a minimization principle for a convex function. From (2.10), however, the Ξ term really contains $|\partial\phi/\partial s\,|^\beta$, so $\int \Xi(\theta-\phi)\,\mathrm{d}x$ is not a monotone operator and cannot be written as a derivative of a convex function. However, this term is always small (note that it is multiplied by $\Delta\rho/\rho_w \approx 0.1$) and we therefore suggest to determine ϕ by iterating Ξ. Starting with a guess for ϕ (Φ, say), Ξ can be calculated (Ξ_Φ, say) and treated as constant while ϕ is calculated from (3.16); then Ξ_Φ is successively updated and used to find improved estimates for ϕ. It is shown in appendix A that this iteration converges provided that the coefficient of Ξ is sufficiently small. In practice, we usually have a good guess as to what the pressure is (from a previous time step, for instance), and require only one or two iterates to attain a reasonable tolerance.

Treating $\Xi = \Xi_\Phi$ as independent of ϕ, (3.16) is equivalent to stating that ϕ minimizes the functional

$$J_\Phi(\phi) := \int_{\Omega^c} \frac{1}{\beta}kh^\alpha|\nabla\phi\,|^\beta + \Lambda(\phi;h) - [m-v_o(h)]\phi\,\mathrm{d}\Omega$$
$$+ \int_{\Gamma^c} \frac{1}{\beta}k_C S^\alpha \left|\frac{\partial\phi}{\partial s}\right|^\beta + \Lambda_C(\phi;S)\,\mathrm{d}\Gamma$$
$$- \int_{\partial\Omega^c\cap\partial\Omega_N} q_N\phi\,\mathrm{d}\Gamma - Q_N\phi|_{\partial\Gamma^c\cap\partial\Omega_N} + \int_{\Gamma^c}\frac{\Delta\rho}{\rho_w}\frac{\Xi_\Phi}{\rho_i L}\phi\,\mathrm{d}\Gamma, \tag{3.17}$$

subject to $\hat{\phi}_m \leqslant \phi \leqslant \hat{\phi}_0$ as well as the imposed Dirichlet boundary conditions (e.g. Ekeland & Temam 1976; Schoof *et al.* 2012), where we have defined

$$\Lambda(\phi;h) := \int_0^{\hat{\phi}_0-\phi} v_c(N',h)\,\mathrm{d}N' \quad\text{and}\quad \Lambda_C(\phi;S) := \int_0^{\hat{\phi}_0-\phi} v_{cC}(N',S)\,\mathrm{d}N'. \tag{3.18}$$

In principle then, (3.17) can be minimized for fixed h and S to find ϕ on $\Omega^c \cup \Gamma^c$. Then ϕ is known everywhere and the appropriate combination of (2.2)–(2.11) can be solved to evolve h, h_w, S and S_w, as described in § 3.2.

3.4. *Summary of the model*

The model can be summarized as follows: at a fixed time t, the subdomains Ω^e, Ω^f, Γ^e and Γ^f can be identified through (3.9) and (3.10). On $\Omega^e \cup \Gamma^e$, $\phi = \hat{\phi}_m$; on $\Omega^f \cup \Gamma^f$, $\phi = \hat{\phi}_0$; and on the remainder, $\Omega^c \cup \Gamma^c$, ϕ is determined as the solution to the variational inequality (3.16), subject to $\hat{\phi}_m \leqslant \phi \leqslant \hat{\phi}_0$ and to the prescribed boundary conditions. The water-filled sheet depth h_w and channel area S_w evolve everywhere according to mass conservation equations (2.4) and (2.11), together with the relevant boundary conditions and jump conditions (2.12). The channel area S evolves everywhere according to (2.8). The sheet depth h evolves according to (2.2) except on those parts of the domain where $\phi = \hat{\phi}_0$, where we have $h = h_w$ instead.

https://doi.org/10.1017/jfm.2012.166 Published online by Cambridge University Press

3.5. *Neglecting hydrostatic terms in the hydraulic potential*

We commented earlier that the hydrostatic terms $\rho_w g h_w$ and $\rho_w g \mathscr{H}_w$ in $\hat{\phi}_0$ and $\hat{\phi}_m$ are typically small, so let us now consider the effect of neglecting them. In that case there is no distinction between ϕ_0 and $\hat{\phi}_0$ or ϕ_m and $\hat{\phi}_m$, and the mass equations on the overpressure and underpressure regions, (2.4) and (2.11), become hyperbolic rather than parabolic. This means that shocks can occur and h_w and S_w no longer have to be continuous. More importantly, it can sometimes present problems balancing fluxes into and out of the channels; if, for example, a channel within an overpressured region is aligned with the direction of the sub-characteristics, $-\nabla\phi_0$, there is no way for the jump condition (2.12) to be satisfied. Indeed, it is clear physically that for water to spread out laterally from such a channel requires a pressure gradient, and that is precisely what the inclusion of the hydrostatic term in $\hat{\phi}_0$ allows for. Similarly, without those diffusive terms, mass conservation at the nodes of the channel network when it is overpressured results in a point source or sink to the sheet, which is problematic.

In practice, when we solve the equations numerically, these troublesome line and point sources are spread out over a discrete cell size. For the situations of interest to us here, this artificial 'diffusion' of the water from channel into sheet is larger than the diffusion that is introduced by the hydrostatic terms in $\hat{\phi}_0$ and $\hat{\phi}_m$. Thus, including those terms adds little to the realism of the solutions; their regularizing effect is already provided by the grid size. We should also remind ourselves that the constraint for the pressure not to exceed overburden is only approximate, and that a finite increase above overburden is required in reality both to cause the uplift of the ice and to drive water out over the bed (Schoof *et al.* 2012). Although we are assuming that these stresses in excess of overburden are small, they may often be larger than the size of ϕ_h, so that including the latter without the other would not be entirely consistent.

For the solutions shown in the next section, we therefore ignore the ϕ_h and $\phi_{\mathscr{H}}$ terms and have the constant bounds, ϕ_m and ϕ_0, on the hydraulic potential. In fact, the issues raised above are of little relevance for the one-dimensional model, which we now focus on.

3.6. *One-dimensional model*

In the one-dimensional version of the model we envisage a single channel that runs in parallel with a sheet occupying a width W, as in figure 4. This can be seen as the subglacial analogue of commonly used flow-line glacier models (e.g. Pimentel & Flowers 2010), and assumes an efficient connection between sheet and channels so that both may be considered at the same width-averaged pressure. The channel is most easily thought of as lying at the centre of the sheet, so that the system can crudely be thought of as representing one catchment basin of a wider array of channels with regular spacing W. In this case the domain is $\Omega = \Gamma \times (-W/2, W/2)$, with $\Gamma = \{x : x \in (0, x_m)\}$, say, and we may take the variables to be defined along Γ. There are analogous projections between Ω^e and Γ^e, and Ω^f and Γ^f, respectively.

A one-dimensional mass conservation equation is derived by integrating the sheet equation (2.4) across the width W, making use of the jump condition (2.12) at the channel, and combining with the the channel equation (2.11):

$$\frac{\partial}{\partial t}[S_w + W h_w] - \frac{\partial}{\partial x}\left[k_C S_w^{\alpha}\left|\frac{\partial \phi}{\partial x}\right|^{\beta-2}\frac{\partial \phi}{\partial x} + W k h_w^{\alpha}\left|\frac{\partial \phi}{\partial x}\right|^{\beta-2}\frac{\partial \phi}{\partial x}\right] = Wm + \frac{\Xi}{\rho_w L}, \quad (3.19)$$

https://doi.org/10.1017/jfm.2012.166 Published online by Cambridge University Press

where we absorb any prescribed inflow from the lateral boundaries into m. This can be interpreted as an equation for the total cross-sectional area $S_w + Wh_w$ across the glacier width, with the advantage that the unknown exchange term κ has been eliminated. The normal evolution equations (2.2) and (2.8) for h and S are

$$\frac{\partial h}{\partial t} = \frac{u_b}{l_r}(h_r - h) - \tilde{A}h|N|^{n-1}N, \tag{3.20}$$

$$\frac{\partial S}{\partial t} = \frac{\Xi}{\rho_i L} - \hat{A}S|N|^{n-1}N, \tag{3.21}$$

and the dissipation term (2.10) is

$$\Xi = k_C S_w^{\alpha} \left|\frac{\partial \phi}{\partial x}\right|^{\beta} + l_r k h_w^{\alpha} \left|\frac{\partial \phi}{\partial x}\right|^{\beta}. \tag{3.22}$$

The combination of (3.19) with (3.20) and (3.21) gives rise to the functional (3.17) that is used to determine ϕ on Γ^c:

$$\begin{aligned} J_\Phi(\phi) := W \int_{\Gamma^c} \frac{1}{\beta} k h^{\alpha} \left|\frac{\partial \phi}{\partial x}\right|^{\beta} + \Lambda(\phi; h) - [m - v_o(h)]\phi \, \mathrm{d}x \\ + \int_{\Gamma^c} \frac{1}{\beta} k_C S^{\alpha} \left|\frac{\partial \phi}{\partial x}\right|^{\beta} + \Lambda_C(\phi; S) + \frac{\Delta\rho}{\rho_w \rho_i L} \Xi_\Phi \phi \, \mathrm{d}x - (W q_N + Q_N)\phi|_{x=0}, \end{aligned} \tag{3.23}$$

where the last boundary terms are present only when Γ^c extends to the inflow boundary at $x = 0$.

Summarizing the problem again: at any fixed t we identify Γ^e and Γ^f from (3.9) and (3.10), on which $\phi = \phi_m$ and $\phi = \phi_0$, respectively (in this width-integrated formulation the definition of Ω^e in (3.9) is redundant). On the remainder of the domain, Γ^c, ϕ is determined by minimizing (3.23) subject to $\phi_m \leqslant \phi \leqslant \phi_0$. Then S_w and h_w evolve everywhere according to (3.19), whilst S evolves according to (3.21) and h evolves according to (3.20) except on those parts of the domain where $\phi = \phi_0$, on which $h = h_w$ instead. The partitioning between S_w and h_w in (3.19) is determined from the fact that $S_w = S$ (when $\phi > \phi_m$), $S_w = 0$ (when $\phi = \phi_m$ and the channel is empty) or $h_w = h$ (when $\phi = \phi_m$ and the channel is partially filled). In the next section we describe the numerical procedure we have implemented to solve this problem.

3.7. *Numerical procedure*

The method we use is similar to that outlined in Schoof *et al.* (2012), using an operator splitting approach to alternatingly (I) find ϕ through the minimization procedure described above and (II) explicitly evolve h, h_w, S and S_w with ϕ held constant. We are currently developing a variant of the same method to use in two dimensions. The procedure is as follows.

(I) For fixed h, h_w, S and S_w, calculate ϕ:
  (*a*) divide Γ into regions Γ^e, Γ^f and Γ^c defined in (3.9)–(3.11);
  (*b*) on Γ^e, assign $\phi = \phi_m$;
  (*c*) on Γ^f, assign $\phi = \phi_0$;
  (*d*) on Γ^c, find ϕ by starting with a guess for Ξ_Φ in (3.22), and iteratively minimizing (3.23) subject to $\phi_m \leqslant \phi \leqslant \phi_0$ and applied Dirichlet conditions, then updating Ξ_Φ.

https://doi.org/10.1017/jfm.2012.166 Published online by Cambridge University Press

(II) With the calculated ϕ, update h, h_w, S and S_w:

(e) based on the computed ϕ, divide the sheet domain into three new regions Γ^+, Γ^- and $\Gamma^0 = \Gamma \setminus (\Gamma^- \cup \Gamma^+)$ defined by (3.4) and (3.5);

(f) on Γ^0, step h forward using (3.20) and set $h_w = h$, and step S forward using (3.21) and set $S_w = S$;

(g) on Γ^+, step S forward using (3.21) and set $S_w = S$, then use the known $\partial S_w/\partial t$ to step h_w forward using (3.19), and set $h = h_w$;

(h) on Γ^-, step h forward using (3.20), and step S forward using (3.21);

(i) on Γ^-, step forward S_w and h_w using (3.19), with the additional constraint that either $h_w = h$ or $S_w = 0$;

(j) some post-processing may be required for Γ^-, where the updated h_w and S_w may not satisfy $h_w \leqslant h$ and $S_w \leqslant S$; the simplest option is simply to set $h_w = h$ and $S_w = S$ in this case, and to move (by altering the computed fluxes) any mass that is neglected in doing so to the neighbouring partially empty region.

The functional (3.23) is discretized using piecewise linear finite elements for ϕ, and the minimization to find ϕ on Ω^c is achieved using either an augmented Lagrangian algorithm or a trust-region method. The discrete ϕ is defined on nodes of a mesh that is also used to define h and h_w. The channel area S is defined on the connecting line segments between those nodes, while it turns out to be helpful to define S_w separately at each end of these channel segments. The normal evolution equations for h and S, which for fixed ϕ are ordinary differential equations, are simply stepped forward explicitly. Where required, the mass conservation equations are also solved with an explicit time step, using a conservative upwind finite volume discretization. The partitioning of water between channels and sheet, in steps (g), (i) and (j) above, is explained in appendix B.

4. One-dimensional results and discussion

4.1. *Steady states*

To demonstrate that the proposed model produces plausible results, we first consider steady-state one-dimensional solutions when the prescribed input m is constant and spatially uniform. This also provides a useful test of the numerical method, since steady solutions can also be found by alternative methods. Those are not entirely straightforward, however, and details of their calculation are given in appendix C. Note, in particular, that there is not necessarily a unique steady-state solution when the sheet width is too wide, although in practice it often is unique, as in the examples shown here.

All of the results in this section assume a spatially uniform meltwater source m. As commented earlier, this represents contributions from basal melting and from surface-derived water that could be calculated as part of a more complete model. It is unlikely that water from the surface should ever realistically be treated as a uniform source, but we nevertheless treat it as uniform for this study because our aim is to assess the generic behaviour of the model.

Figure 5 shows steady-state solutions for ϕ, h, h_w, S and S_w, as well as the corresponding channel and sheet discharges, for four different constant melt inputs, using the glacier geometry shown in figure 1; that is, a 'plastic' ice shape determined from $-\rho_i g H \partial(b + H)/\partial x = \tau_c$, with $b(x)$ a linear slope 50 km long and 1000 m high, and $\tau_c = 10^5$ Pa. The sheet width W is 200 m, and the other parameters used are shown in table 1. The geometry and values chosen are intended to be loosely

https://doi.org/10.1017/jfm.2012.166 Published online by Cambridge University Press

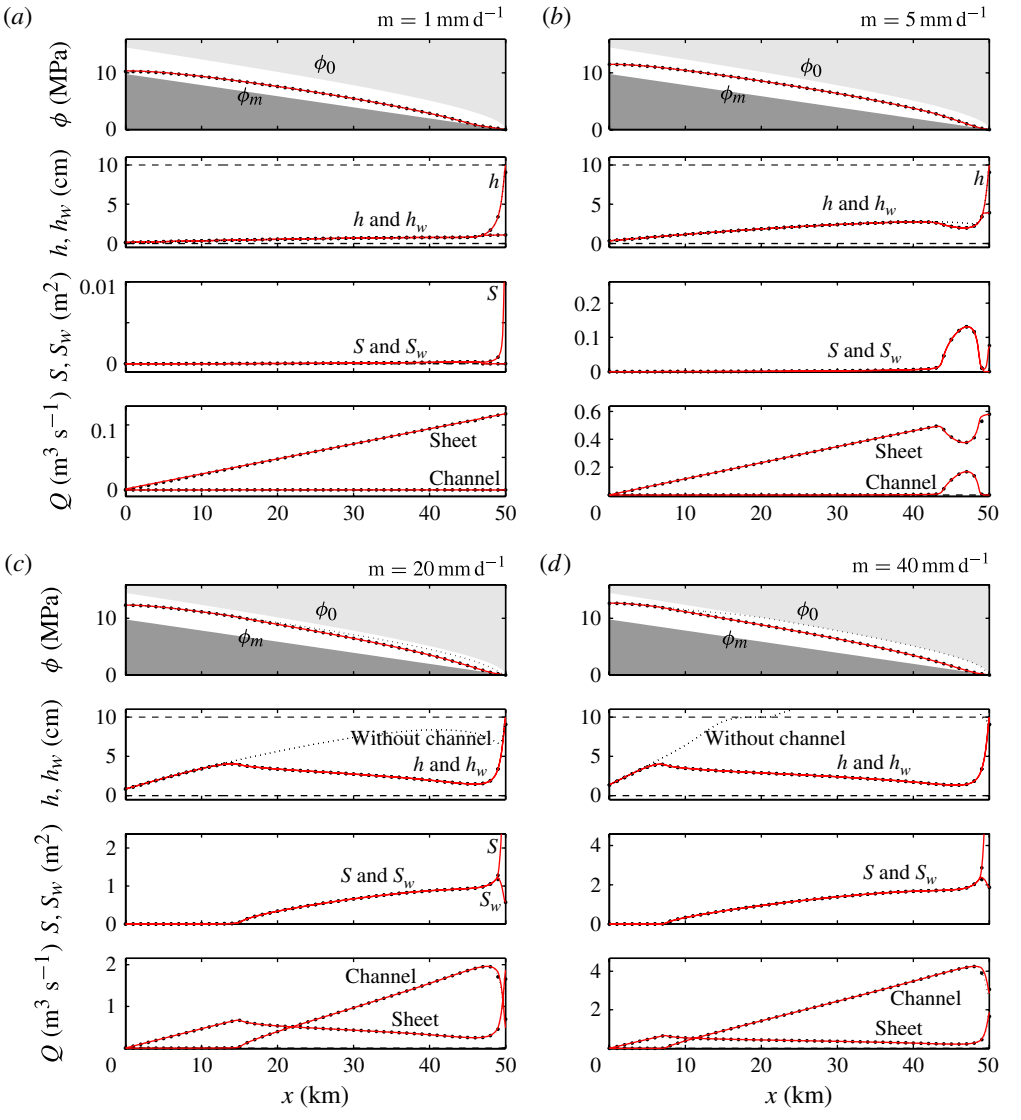


FIGURE 5. (Colour online) Steady-state solutions for the hydraulic potential ϕ, sheet depth h and water-filled depth h_w, channel area S and water-filled area S_w, and total discharge Q in channel and sheet. Solutions are shown for four different constant melt inputs m: (*a*) 1, (*b*) 5, (*c*) 20 and (*d*) 40 mm d^{-1}; and $q_N = Q_N = 0$ at $x = 0$. Note the different axes scales in each case. Dots show numerical solutions, while solid lines (red in the online version of this article) show solutions by ordinary differential equation methods described in appendix C; they are mostly indistinguishable. The smaller dotted lines show the corresponding solutions for ϕ and h without allowing for a channel (Schoof *et al.* 2012), in which case both h and ϕ are larger. Shaded regions for ϕ correspond to $\phi < \phi_m$ and $\phi > \phi_0$. Note that drainage through the channel begins further upglacier for larger melt input and that the drainage system is always full except close to the margin.

appropriate for a large valley glacier, or perhaps the edge of the Greenland ice sheet. We note that there is significant uncertainty in some of the parameters, particularly

https://doi.org/10.1017/jfm.2012.166 Published online by Cambridge University Press

ρ_w	1000 kg m^{-3}	β	3/2	h_r	0.1 m
ρ_i	910 kg m^{-3}	n	3	l_r	2 m
g	9.8 m s^{-1}	k	0.01 m$^{7/4}$ kg$^{-1/2}$	$\tilde{A}$	5×10^{-25} Pa^{-3} s^{-1}
α	5/4	k_C	0.1 m$^{3/2}$ kg$^{-1/2}$	$\hat{A}$	5×10^{-25} Pa^{-3} s^{-1}
		u_b	30 m y^{-1}		

TABLE 1. Values of the physical parameters in the model used in § 4. Values of α, β and k_C are based upon the Darcy–Weisbach parameterization of flow through small semicircular conduits; values of $\tilde{A}$ and $\hat{A}$ are taken as $2A/n^n$, assuming semicircular cavities and channels, with $A \approx 6.8 \times 10^{-24}$ Pa^{-3} s^{-1} appropriate for ice at 0 °C (Paterson 1994). Values for k, h_r and l_r are less well known, and those used here are chosen as seemingly sensible values (giving an average water speed through the full sheet of around 5 cm s^{-1} on a 1° slope). Sliding speed u_b should really be determined by considering the overlying ice flow and the constant used here is chosen as a representative value.

the bed roughness scales h_r and l_r, and sheet permeability k. The values used here seem plausible, but one should be wary of applying these same parameters to any particular geographical location without attempting some form of fit to available observations.

In each case, the dots show the numerical solutions and the solid lines (red in the online version of this articles) show the steady-state calculated directly as described in appendix C. Where there are two lines on the h and S plots, the lower is h_w or S_w; where there is only one line it indicates that $h_w = h$ or $S_w = S$. For comparison we also show the solutions for ϕ and h in the case when there is no channel. As expected, the presence of the channel reduces both the sheet depth h and the water pressure.

Also as expected, the larger the discharge the further up the glacier the channel forms, and the larger the proportion of water transported in the channel. Note that when the channel is sufficiently small, in figure (*b*), the water does not remain in it all of the way to the margin but transfers back out into the sheet. This behaviour is due to the small effective pressure at the margin which implies, from (2.2), that h becomes large and the sheet therefore has a large carrying capacity. For the larger inputs, however, the channel does extend to the margin, becoming partially empty close to the edge.

Figure 6 shows similar steady solutions for a thin glacier with a stepped bed and surface profile (as before, the glacier geometry can be seen from the shaded regions showing ϕ_m and ϕ_0). Again, four different melt inputs are considered. At the lowest, the sheet is everywhere only partially full and the channel is always empty. As the discharge is increased, the sheet and channel first become water filled in the regions with shallow potential gradient. Note too that the channel area, even when it is only small in (*a*) and (*b*), is typically larger in sections with a steep potential gradient where there is consequently greater dissipation. For the larger discharges in (*c*) and (*d*) the sheet is always full, but the channel remains only partially filled in the steeper sections, where its total area is larger as a result of the greater dissipation.

4.2. *Diurnal meltwater variation*

In figure 7, we show solutions for the same glacier geometry as in figure 5, when the meltwater input varies sinusoidally over two diurnal periods (it is still spatially uniform). These solutions are approximately periodic, having been allowed to adjust previously from an initial steady state for the mean input. The timing is such that $t = 0$

https://doi.org/10.1017/jfm.2012.166 Published online by Cambridge University Press

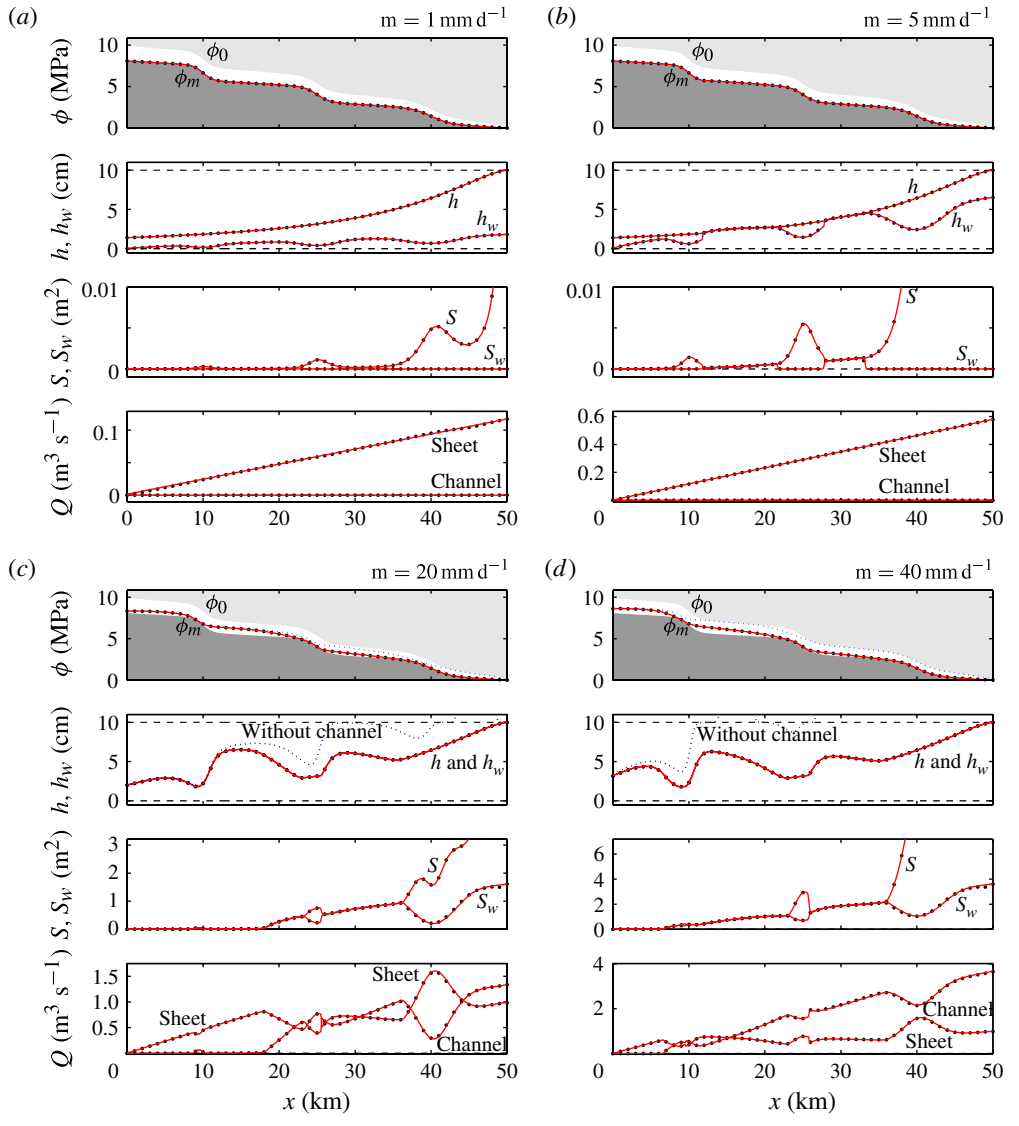


FIGURE 6. (Colour online) Steady-state solutions as in figure 5 but for a stepped glacier profile indicated by the shaded regions for ϕ, and for four different uniform melt inputs m, as shown. Note the different axes scales in each case. Small dotted lines on the plots for ϕ and h show the solution when there is no channel. Channel area S is always largest beneath steep sections of the ice. At low discharge the channel is empty and the sheet is only partially filled; for increasing discharge the sheet and channel fill up (initially beneath shallow slopes), although the channel remains partially empty beneath steep sections and beneath the thin ice near the margin.

corresponds to lowest melt input to the bed; that will likely lag behind the time of least melting on the surface, depending on how efficient the connection is from the surface (Shepherd *et al.* (2009), for instance, infer a lag of 2 hours during the summer on the Russel Glacier in western Greenland).

https://doi.org/10.1017/jfm.2012.166 Published online by Cambridge University Press

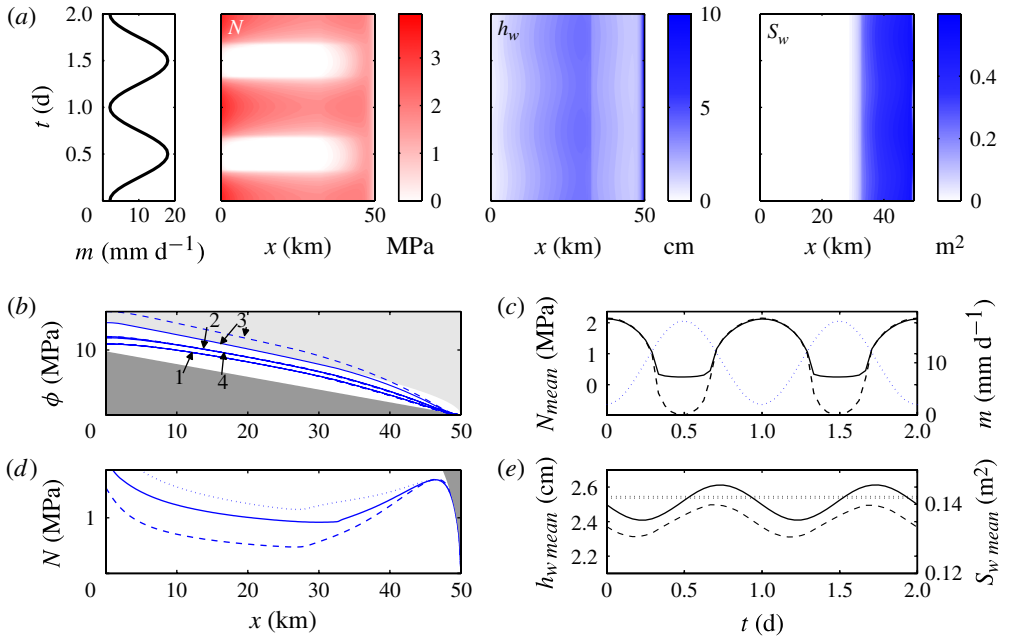


FIGURE 7. (Colour online) (*a*) Periodic solutions for a sinusoidally varying meltwater input, $m = 10 - 8\cos(2\pi t/t_d)$ mm d^{-1}, where $t_d = 1$ d, for the same glacier geometry and other parameters as shown in figure 5. (*b*) Profiles of the hydraulic potential at equally spaced time intervals corresponding to (i) minimum input, (ii) increasing input, (iii) maximum input and (iv) decreasing input (almost identical to (ii)), with solid lines showing the constrained solution, dashed lines showing the equivalent solution with no constraints on the pressure. (*c*) Variation with time of the mean effective pressure (constrained solution, solid; unconstrained solution, dashed) and melt input (dotted), averaged over the whole length of the glacier. (*d*) Profiles of the average effective pressure over the whole diurnal period, according to the constrained solution (solid) and the unconstrained solution (dashed), with the dotted line showing the pressure profile if the melt input were constant at the mean. (*e*) Variation with time of the mean sheet depth (solid) and channel area (dashed), averaged over the whole length of the glacier. Dotted lines show the case of constant input.

There are several important things to note from figure 7. First, the effective pressure reaches zero ($\phi = \phi_0$) during the periods of largest melt input. It does not become negative, since that is not allowed by the model, but remains at zero until the inflow reduces again. For comparison, figure 7(*b*) shows the hydraulic potential at four instances during the cycle, together with the profiles that are predicted using the same model but without the modifications when $\phi \geqslant \phi_0$ (the model therefore allows for creep opening, rather than uplift). There is very little difference during the normal pressure periods, when the models are the same, but the unconstrained model naturally predicts pressure well in excess of overburden during the time of peak input. This is also shown in figure 7(*c*), which shows how the effective pressure averaged over the whole bed varies with time, and compares the constrained model (solid) with the unconstrained one (dashed).

The temporal average of the effective pressure profile is shown in figure 7(*d*): again the solid line shows the prediction of the current model, the dashed line shows the equivalent result for the unconstrained model, and the dotted line in this case shows

https://doi.org/10.1017/jfm.2012.166 Published online by Cambridge University Press

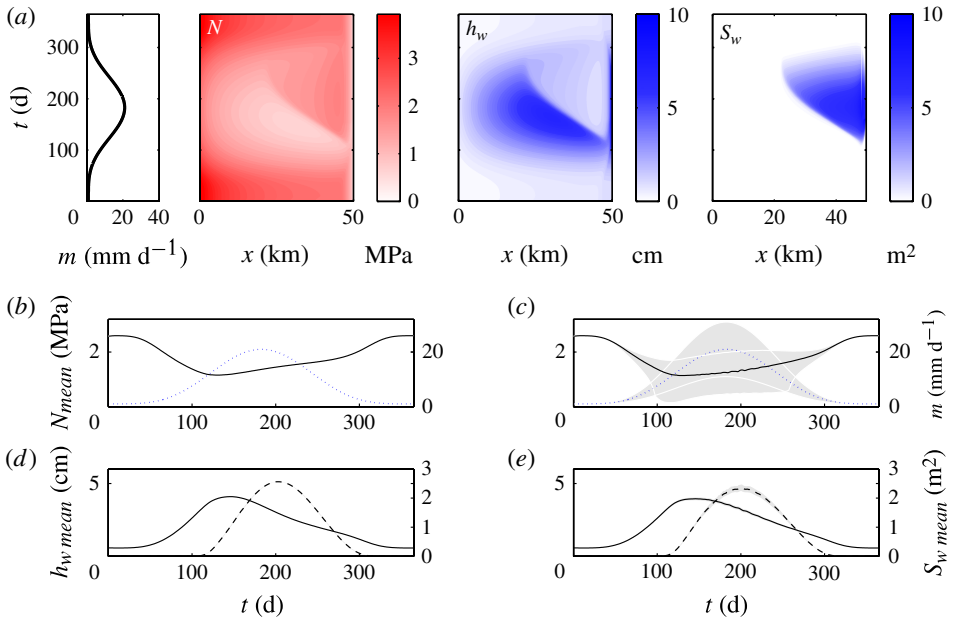


FIGURE 8. (Colour online) (*a*) An idealized annual melt cycle for the same glacier geometry as shown in figure 5, except $W = 2$ km, with $m = 1 + 20\sin^4(2\pi t/t_y)$ mm d^{-1}, where $t_y = 1$ y. Note the growth of channels upglacier during the course of the summer, and resulting increase in effective pressure in those regions. (*b*) Variation with time of the effective pressure averaged over the glacier length (solid), and the melt input (dotted). (*d*) Variation with time of the sheet depth (solid) and channel area (dashed), averaged over the glacier length. (*c*) and (*e*) show the same averages as in (*b*) and (*d*), when the amplitude of the melting varies diurnally, $m = 1 + 10(2 - \cos(2\pi t/t_d))\sin^4(2\pi t/t_y)$ mm d^{-1}, with lines showing diurnal averages and shaded areas showing the diurnal range.

what the average would be if the melt input were not varying but were constant at the mean. In this case, the average N is lower when the input is varying, although the constraint on N becoming negative means it is not as low as it would be in the unconstrained case.

It is notable in figure 7(*a*) that the sheet depth and channel area do not change very much. This is because the diurnal time scale is faster than the natural time scales for opening and closing associated with (2.2) and (2.8), so gives them little time to adjust (faster uplift of the sheet is possible during the high-pressure period, but the melt rates imposed are not sufficient to cause large variations). Nevertheless, there is some variability in both S_w and h_w, and their average over the length of the glacier is shown in figure 7(*e*). Note that the time of peak melt, during which there is high pressure, correlates with the time of maximum rate of change of water storage (h_w). This is fundamentally different from poroelastic sheet models which instead predict the largest storage at that time.

4.3. *Annual cycle*

Figure 8 shows the evolution of the one-dimensional drainage system due to an idealized annually varying meltwater input (the width is 10 times larger than in figure 5, $W = 2$ km, so that a significant channel can develop). When the input is

https://doi.org/10.1017/jfm.2012.166 Published online by Cambridge University Press

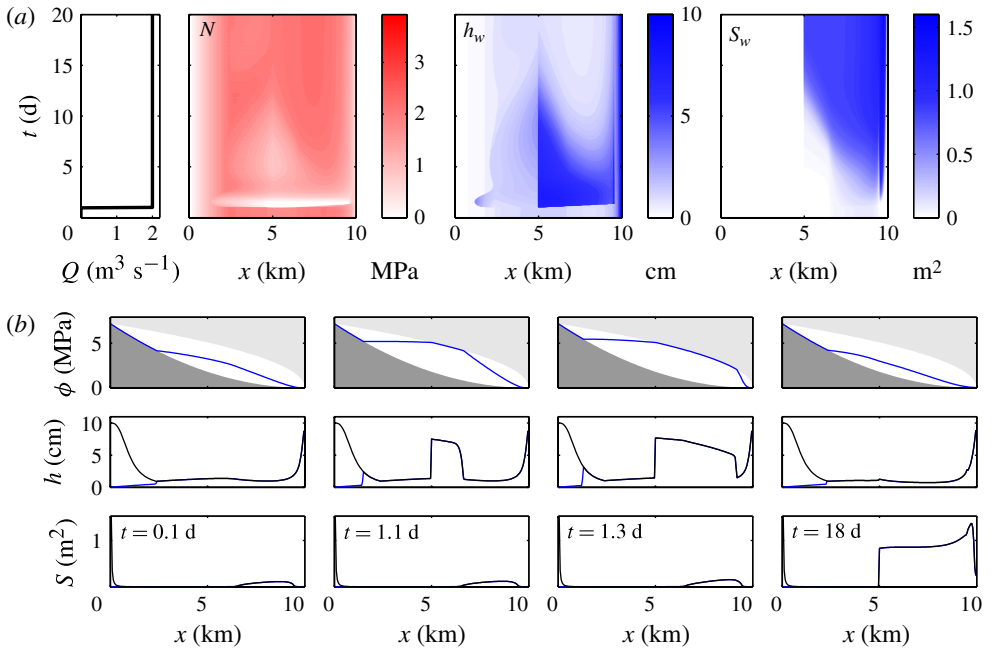


FIGURE 9. (Colour online) (*a*) Response of the drainage system to a sudden point source $Q = 2\ \mathrm{m^3\ s^{-1}}$ opening at time 1 d at $x = 5$ km, with a uniform background melting rate $m = 20\ \mathrm{mm\ d^{-1}}$ that remains constant throughout. The glacier geometry is shown by the shaded regions in the plots for ϕ in (*b*), which correspond to ϕ_m and ϕ_0. (*b*) Profiles of hydraulic potential, sheet depth and channel area before the additional source starts and at three later times as shown.

at its lowest, in winter, the channel is extremely small. As melting increases the sheet initially enlarges, followed by the channel, which starts growing from near the margin where the discharge is greatest. As the channel takes over transporting more of the water, the sheet depth decreases and the effective pressure increases. The lowest effective pressure at any given location is therefore just before channelization occurs (see figure 8*a*).

The melt input in this situation varies sufficiently slowly that the pressure never reaches overburden, and open-water flow only occurs very close to the margin during the winter. If shorter time scale variability of m is included then the pressure varies much more rapidly and overpressure often occurs. The averages over the length of the glacier in such a case are shown in figure 8(*c*) and (*e*), where the large range of the effective pressure can be seen.

4.4. *Sudden meltwater increase*

Figure 9 shows an example of a rapid change in meltwater source, such as might happen when a crevasse or moulin suddenly opens to provide a hydraulic connection between surface and bed. In this case, the drainage system is initially in a steady state (shown in the first column of figure 9*b*) that results from a constant uniform source. After 1 day, an additional point source is initiated half way along the glacier. There is a rapid increase to overburden at the injection site, and the water initially spreads both up and down glacier in the porous sheet, causing uplift of the ice downstream (see

https://doi.org/10.1017/jfm.2012.166 Published online by Cambridge University Press

figure 9*b*). The channel is initially unaffected, but over the next few days the greater discharge causes the channel downstream of the injection site to grow, and the sheet slowly collapses again.

Water pressure is sustained at overburden over a significant portion of the bed for around 12 hours after the onset, before subsiding again. If the rapid uplift of the sheet had not been allowed for in the model, and only creep opening instead, the pressure would have become much higher than overburden locally, and there would not have been the same downslope front propagation.

The method of allowing for uplift in our model is not strictly appropriate, however, to the initial stages of this injection, when uplift occurs very locally. On these short time scales, such uplift would be resisted by elastic stresses in the ice, which we have assumed to be negligible compared with the overburden pressure. To lift up a section of ice with lateral dimension $L \approx 200$ m by $h \approx 5$ cm would induce an elastic stress on the order of $E/(1-\nu^2) \times h/L \approx 1.7$ MPa (taking Young's modulus $E = 6.2$ GPa and Poisson's ratio $\nu = 0.3$), which is not insignificant. When the uplifted region is larger, say $L \approx 2$ km, the stress would be around 0.17 MPa, and its neglect becomes less important (the ice also deforms more viscously on time scales longer than a few hours). These additional stresses should in reality smooth out the steep edges of the uplifted region in figure 9, however. A hydrofracture model such as that presented by Tsai & Rice (2010) could be used to model the initial period of injection, whilst the current model is more appropriate for the longer time scale behaviour. Allowing the water to spread out rapidly initially, as in figure 9, nevertheless seems more realistic than requiring excessively high pressures to expand the sheet by viscous creep.

A similar issue regarding short time scales may be relevant to the case of diurnal fluctuations in § 4.2; the Maxwell time, over which the ice behaves more elastically than viscously, is typically estimated to be a few hours. For the smooth meltwater variations in figure 7, with minimal resulting uplift (of the order of a millimetre), the elastic stresses are unlikely to be relevant. If the input has more short term and spatial variability, however, the model may not be so appropriate.

5. Conclusions

We have presented a model of a subglacial channel network that overlies a sheet description of distributed drainage, thus combining aspects of existing continuum and discrete models. The advantage over discrete models is that one does not have to resolve individual drainage elements that may occur on the scale of bed roughness, which is often too small to be practically incorporated into ice-sheet models. The advantage over continuum models is that channelized transport can be included without having to prescribe the location and spacing of channels; rather, the spacing of a potential channel network is prescribed, and the location of the real channel segments within that is selected dynamically.

Our main emphasis in §§ 3 and 4 has been on the complications associated with water pressure exceeding overburden or becoming negative. It is worth pointing out, however, that the model in § 2 can be used as it stands if one is not concerned with those limits (perhaps because there is little short-term variability and the ice is sufficiently thick). That model is relatively simple, consisting of evolution and mass conservation equations for the sheet (equations (2.2) and (2.4)) and for each potential channel segment (equations (2.8) and (2.11)). Combined, they can be cast as an elliptic equation for the water pressure, coupled to local evolution equations for sheet depth and channel area.

https://doi.org/10.1017/jfm.2012.166 Published online by Cambridge University Press

To account for the different behaviour when overburden pressure or zero pressure are reached, however, the additional physical considerations we have included are to allow for arbitrary separation of the ice from the bed when 'overpressure' is attained, and to allow for channels and cavities to be only partially filled when 'underpressure' is attained. The hydraulic potential is constrained to lie at or between the bounds $\hat{\phi}_0$ and $\hat{\phi}_m$ corresponding to overburden and zero pressure, and this allows the potential to be calculated by means of the constrained variational problem in § 3.3.

Our one-dimensional results show that the model gives quite plausible predictions. Underpressure is common when discharge is relatively low, beneath steeper and thinner ice, and at the mouth of channels that extend to the glacier margin. Overpressure occurs when there are rapid changes in meltwater input. Channels extend further up glacier when there is a larger discharge and, other things being equal, tend to be larger beneath steeper ice where there is enhanced dissipative heating.

It is worth pointing out some differences between this model and the work of Schuler & Fischer (2009), who similarly accounted for partially empty channels. Unlike that work, we make no modification to the flow parameterization when the sheet or channel become partially empty. The frictional resistance resulting from turbulent stresses may depend on whether the water makes direct contact with the ice wall or with an intervening air-filled gap, but we consider this a secondary effect that we neglect, and maintain the lumped flow parameterization in (2.9) throughout. Note also, if comparing with Schuler & Fischer (2009), that the dissipation term (2.10) is unaltered when the channel is only partially filled (although the distinction between S and S_w becomes relevant), since we still assume instantaneous transfer of heat to the ice walls.

The numerical method we have devised uses an explicit time step to evolve the sheet depth and channel area, together with the variational formulation to solve for the pressure at each step. Although this scheme is successful at matching steady-state solutions that have been calculated by other means, it has a number of drawbacks. Chiefly, the explicit time stepping puts restrictions on the size of time steps that must be taken, which can be quite severe, particularly when the hyperbolic transport equations must be solved (e.g. LeVeque 2002): when underpressure occurs, the water-filled sheet depth and channel area evolve according to (2.4) and (2.11) and the time step is then limited by the CFL condition (the same occurs for the overpressured sheet, although this is less of a problem since the velocity in the sheet is typically much smaller). If the diffusive term $\rho_w g h_w$ in the potential $\hat{\phi}_m$ were included it would also impose a more stringent restriction as the grid size is refined.

An additional difficulty with the computations is dealing with the boundaries of the overpressure and underpressure regions. At a given fixed time, the variational method to solve for ϕ calculates these automatically; but as soon as time evolution is introduced and discrete elements of the mesh start moving in and out of the contact domain Ω^c, correctly accounting for the migration of the boundaries becomes a somewhat delicate matter. One must take care to ensure that mass is conserved despite different discretizations for fluxes being necessary on the different regions. Ideally, one might hope to construct an implicit or semi-implicit method that takes account of the varying h and S (and also h_w and S_w) at the same time as calculating ϕ. An improved method must await further work, however.

Aside from the technicalities of solving the model, its greatest deficiency is probably the restriction of the pressure to overburden. We have assumed that the required rates of uplift, $\partial h/\partial t$, are achieved with insignificant excess pressure above overburden. As

https://doi.org/10.1017/jfm.2012.166 Published online by Cambridge University Press

discussed in Schoof *et al.* (2012), this is often the case when the overpressured region has significant lateral extent, in which case the viscous resistance to uplift is small. It is not true, however, when only a small region is pressurized or when the uplift rate is much larger than usual, in which case significant stresses in the ice, both viscous and elastic, may have to be overcome. Allowing for this possibility presents quite a challenge for the present model, however, since determining those excess pressures is a non-local problem. Situation-specific hydrofracture or beam-type models could be used (e.g. Pimentel & Flowers 2010; Tsai & Rice 2010), but it is not yet clear how to integrate such approaches into a more general framework.

We are currently working to extend the results to two dimensions, with a disordered arrangement of potential channels, and to include the hydrostatic contribution to the hydraulic potential. Apart from allowing more realistic simulations, this should enable us to determine likely channel spacings, and to test the model's sensitivity to the density of the imposed channel network (it is hopefully clear that the maximum cross-sectional area of the channels in the one-dimensional results in § 4 is simply set by the prescribed width W, whereas the two-dimensional network should select the channel size automatically; see Schoof (2010) and Hewitt (2011)).

We also hope to use the model to examine the effects of short- and long-term variability of the melt input on the effective pressure and hence on glacier sliding. We refrain from making general predictions at this stage, since the implications likely depend upon the precise geometry and forcings, and may require better calibration of the model parameters. In figure 7, for instance, we saw that accounting for diurnal melt variability resulted in a reduction of mean effective pressure, but this is for a specific case when the majority of water is contained in the sheet and it is not clear whether the same result holds true in general.

Acknowledgements

I.J.H. gratefully acknowledges the support of a Killam postdoctoral fellowship at the University of British Columbia. C.S. was supported by a Canada Research Chair and NSERC Discovery Grant number 357193 and NSERC Northern Research Supplement 361960. M.A.W. thanks the Swiss National Science Foundation for support through a Fellowship for Prospective Researchers (grant no. PBEZP2-127812). We thank G. Flowers and J. Ferguson for discussions, and three anonymous referees for their helpful comments.

Appendix A. Proof of convergence of Picard iteration for small density difference

In this appendix, we study the non-monotone variational inequality (3.16) and its numerical solution. We assume that Γ^c is a set of piecewise C^1 arcs. Let $\bar{\Omega}^c = \Omega^c \cup \Gamma^c$ and assume that $\bar{\Omega}^c$ is a bounded, open set with a Lipshitz boundary $\partial\bar{\Omega}^c$, with Γ^c in its interior. The appropriate function space V to cast the problem in is the completion of $C^2(\bar{\Omega}^c) \cap C^0(\partial\bar{\Omega}^c)$ with respect to the norm

$$\|\phi\|_V = \int_{\bar{\Omega}^c} |\phi|^\beta + |\nabla\phi|^\beta \, \mathrm{d}\Omega + \int_{\Gamma^c} |\phi|^\beta + \left|\frac{\partial\phi}{\partial s}\right|^\beta \, \mathrm{d}s. \tag{A 1}$$

In other words, $V = \{\phi \in W^{1,\beta}(\bar{\Omega}^c) : \gamma(\phi) \in W^{1,\beta}(\Gamma^c)\}$ where γ is the relevant trace operator. As a closed subspace of $L^\beta(\bar{\Omega}^c) \times L^\beta(\bar{\Omega}^c) \times L^\beta(\Gamma^c) \times L^\beta(\Gamma^c)$, this is a reflexive Banach space with respect to the norm $\|\cdot\|_V$. We also denote by V_D the

https://doi.org/10.1017/jfm.2012.166 Published online by Cambridge University Press

affine subspace of functions that satisfy the relevant Dirichlet conditions, and define the convex, closed set $K = \{\phi \in V_D : \hat{\phi}_m \leqslant \phi \leqslant \hat{\phi}_0 \text{ almost everywhere}\}$ of admissible functions in (3.16). For simplicity, we assume that Dirichlet conditions hold on some part of $\partial\bar{\Omega}^c$, so Poincaré's inequality can be applied.

We also assume that $h \in L^\infty(\bar{\Omega}^c) \cap L^\infty(\Gamma^c)$, $S \in L^\infty(\Gamma^c)$ with $h > h_0 > 0$ and $S > S_0 > 0$ for some constants h_0 and S_0, and that $\hat{\phi}_m, \hat{\phi}_0 \in L^\infty(\bar{\Omega}^c) \cap L^\infty(\Gamma^c)$, with $\hat{\phi}_m$ and $\hat{\phi}_0$ such that K is non-void. In addition, assume that $v_c(N, h)$ and $v_{cC}(N, S)$ are bounded below by 0 for $N > 0$ and strictly increasing in their first argument, and that $v_c(\hat{\phi}_0 - \phi, h)$ as well as $v_{cC}(\hat{\phi}_0 - \phi, S)$ are measurable for all $\phi \in K$ with $v_c(\hat{\phi}_0 - \hat{\phi}_m, h) \in L^{\beta/(\beta-1)}(\bar{\Omega}^c)$, $v_{cC}(\hat{\phi}_0 - \hat{\phi}_m, S) \in L^{\beta/(\beta-1)}(\Gamma^c)$. Note that this ensures that $\int_{\Omega^c} \Lambda(\phi, h)\,\mathrm{d}\Omega$ and $\int_{\Gamma^c} \Lambda_C(\phi, h)\,\mathrm{d}\Omega$ are both bounded on K. Moreover, we require that $m, v_o(h) \in L^\beta(\bar{\Omega}^c)$, $q_n \in L^\beta(\partial\bar{\Omega}^c \cap \partial\Omega_N)$. These assumptions allow us to apply standard methods from convex analysis (Ekeland & Temam 1976) to the problem at hand.

We now turn to the offending term $\int_{\Gamma^c} \Xi(\theta - \phi)\,\mathrm{d}\Gamma$ in (3.16). This corresponds to the non-monotone operator

$$B(\Phi, \phi) = \int_{\Gamma^c} (k_C S^\alpha + l_r k h^\alpha) \left|\frac{\partial \Phi}{\partial s}\right|^\beta \phi \,\mathrm{d}\Gamma. \tag{A 2}$$

First we show that $B(\Phi, \cdot)$ is a bounded linear operator on V for every $\Phi \in V$. Given that, we can then define a mapping $F(\Phi) = \arg\min_{\phi \in K} J_\Phi(\phi)$, where

$$\begin{aligned} J_\Phi(\phi) := &\int_{\Omega^c} \frac{1}{\beta} k h^\alpha |\nabla\phi|^\beta + \Lambda(\phi; h) - [m - v_o(h)]\phi \,\mathrm{d}\Omega \\ &+ \int_{\Gamma^c} \frac{1}{\beta} k_C S^\alpha \left|\frac{\partial\phi}{\partial s}\right|^\beta + \Lambda_C(\phi; S)\,\mathrm{d}\Gamma \\ &- \int_{\partial\Omega^c \cap \partial\Omega_N} q_N \phi \,\mathrm{d}\Gamma - Q_N\phi|_{\partial\Gamma^c \cap \partial\Omega_N} + \nu B(\Phi, \phi) \end{aligned} \tag{A 3}$$

with $\nu = \Delta\rho/(\rho_w \rho_i L)$. Here J_Φ is strictly convex, weakly lower-semicontinuous and, by Poincaré's inequality, coercive on K and hence has a unique minimizer, so $F(\Phi)$ is well defined. Then $\phi = F(\Phi)$ also satisfies the variational inequality

$$\begin{aligned} &\int_{\Omega^c} k h^\alpha |\nabla\phi|^{\beta-2} \nabla\phi \cdot \nabla(\theta - \phi) - v_c(\hat{\phi}_0 - \phi, h)(\theta - \phi) - [m - v_o(h)](\theta - \phi)\,\mathrm{d}\Omega \\ &\quad + \int_{\Gamma^c} k_C S^\alpha \left|\frac{\partial\phi}{\partial s}\right|^{\beta-2} \frac{\partial\phi}{\partial s} \frac{\partial(\theta - \phi)}{\partial s} - v_{cC}(\hat{\phi}_0 - \phi, S)(\theta - \phi)\,\mathrm{d}\Gamma \\ &\quad - \int_{\partial\Omega^c \cap \partial\Omega_N} q_N(\theta - \phi)\,\mathrm{d}\Gamma - Q_N(\theta - \phi)|_{\partial\Gamma^c \cap \partial\Omega_N} + \nu B(\Phi, \theta - \phi) \geqslant 0, \end{aligned} \tag{A 4}$$

for all $\theta \in K$, and it is clear that solving (3.16) therefore amounts to finding a fixed point of F. To this end, we show below that F is a contraction mapping on a suitable subset of K for sufficiently small ν. This then ensures the existence at least of a locally unique fixed point, and also that the Picard iteration in § 3.7 converges for suitable initial guesses.

Note that Γ^c is one-dimensional. With $\beta > 1$, $W^{1,\beta}(\Gamma^c) \subset C(\Gamma^c)$ follows by Morrey's inequality, with $\|\phi\|_{C(\Gamma^c)} \leqslant C_1 \|\phi\|_{W^{1,\beta}(\Gamma^c)} \leqslant C_1 \|\phi\|_V$ for some constant C_1

https://doi.org/10.1017/jfm.2012.166 Published online by Cambridge University Press

that depends only on β and the geometry of Γ^c. Hence,

$$|B(\Phi,\phi)| \leqslant C_2 \|\Phi\|^{\beta}_{W^{1,\beta}(\Gamma^c)} \|\phi\|_{C(\Gamma^c)} \leqslant C_1 C_2 \|\Phi\|^{\beta}_{V} \|\phi\|_{V}, \tag{A 5}$$

where C_2 depends only on h_0, S_0 and various fixed parameters such as α, but not on ν. This shows that $B(\Phi,\cdot)$ is a bounded linear functional.

Next, we show that for small enough ν there is a non-void, closed and bounded set $K_0 \subset K$ such that $F : K_0 \mapsto K_0$. Pick a representative $\phi_r \in K$; for definiteness, this can be the smallest element of K with respect to the norm $\|\cdot\|_V$. We know that $J_\Phi(\phi) \leqslant J_\Phi(\phi_r)$. After manipulating using (A 5) and Poincaré's inequality and the fact that the integrals $\int_{\Omega^c} \Lambda(\theta,h)\,\mathrm{d}\Omega$ and $\int_{\Gamma^c} \Lambda_C(\theta,h)\,\mathrm{d}\Omega$ are both bounded on K, we find

$$C_3\|\phi\|^{\beta}_{V} - \nu C_1 C_2 \|\Phi\|^{\beta}_{V}\|\phi\|_{V} \leqslant C_4\|\phi_r\|^{\beta}_{V} + C_5 + \nu C_1 C_2 \|\Phi\|^{\beta}_{V}\|\phi_r\|_{V}. \tag{A 6}$$

Here C_3, C_4 and C_5 are positive constants that depend on the domain as well as various parameters and data functions such as α, h, S m, v_o etc as well as on the bounds on the integrals of Λ and Λ_C; they are independent of ϕ, ϕ_r, Φ and ν, and we have $C_3 \leqslant C_4$. From (A 6) it is straightforward to show that, for sufficiently small ν, we get the bound $\|\phi\|_V \leqslant R_0$ when $\|\Phi\|_V \leqslant R_0$, where $R_0 = 2\,(C_4/C_3)^{1/\beta}\,\|\phi_r\|_V + (C_5/C_3)^{1/\beta}$ is independent of ν. We can then pick $K_0 = \{\phi \in K : \|\phi\|_V \leqslant R_0\}$, which necessarily contains ϕ_r and is therefore non-void.

Next, we show that F is a contraction mapping on K_0 for small ν. Let $\phi_1 = F(\Phi_1)$ and $\phi_2 = F(\Phi_2)$. In turn, let $\Phi = \Phi_1$ with $\theta = \phi_2$ and $\Phi = \Phi_2$ with $\theta = \phi_1$ in (A 4), and add the resulting inequalities. After some manipulation and bearing in mind that v_c and v_{cC} are increasing functions of $N = \hat{\phi}_0 - \phi$, we get

$$\begin{aligned}
&\int_{\Omega^c} kh^{\alpha}(|\nabla\phi_2|^{\beta-2}\nabla\phi_2 - |\nabla\phi_1|^{\beta-2}\nabla\phi_1)\cdot\nabla(\phi_2-\phi_1) - \,\mathrm{d}\Omega \\
&\qquad + \int_{\Gamma^c} k_C S^{\alpha}\left(\left|\frac{\partial\phi_2}{\partial s}\right|^{\beta-2}\frac{\partial\phi_2}{\partial s} - \left|\frac{\partial\phi_1}{\partial s}\right|^{\beta-2}\frac{\partial\phi_1}{\partial s}\right)\frac{\partial(\phi_2-\phi_1)}{\partial s}\,\mathrm{d}\Gamma \\
&\qquad \leqslant \nu[B(\Phi_2,\phi_2-\phi_1) - B(\Phi_1,\phi_2-\phi_1)].
\end{aligned} \tag{A 7}$$

Typical turbulent closure schemes lead to $\beta = 3/2$ so we assume $1 < \beta \leqslant 2$. By well-established stability estimates (Glowinski 1984) and Poincaré's inequality, this implies

$$\begin{aligned}
C_6\,(\|\phi_1\|_V + \|\phi_2\|_V)^{\beta-2}\,\|\phi_2-\phi_1\|^2_V &\leqslant \nu[B(\Phi_2,\phi_2-\phi_1) - B(\Phi_1,\phi_2-\phi_1)] \\
&\leqslant \nu C_1 C_2 \beta 2^{\beta-1}\,(\|\Phi_1\|_V + \|\Phi_2\|_V)^{\beta-1}\,\|\Phi_2-\Phi_1\|_V\,\|\phi_2-\phi_1\|_V
\end{aligned} \tag{A 8}$$

where $C_6 > 0$ depends only on domain geometry and the parameters β, α, h_0 and S_0. For Φ_1, $\Phi_2 \in K_0$, we also have ϕ_1, $\phi_2 \in K_0$ and their norms are bounded independently of ν. With all other parameters fixed and a given domain shape, it follows that $\|F(\Phi_2) - F(\Phi_1)\|_V = \|\phi_2-\phi_1\|_V < r\|\Phi_2-\Phi_1\|_V$ where r is a constant that, for small enough ν, is less than unity, and we have a contraction mapping.

In the proof above, it is essential that the domain be finite (so Poincaré's inequality holds), and the required smallness of ν will depend on domain size through constants such as C_3, C_4 and C_6. In fact, for large domains, one should expect channel flow potentially to exhibit pathological behaviour. Consider (3.13) with channel discharge defined as $Q = k_C S^{\alpha}|\partial\phi/\partial s|^{\beta-2}\,\partial\phi/\partial s$ and Ξ given by (2.10). At a fixed point in time (so that S_w and h_w can be treated as fixed), we then have a problem that behaves at

https://doi.org/10.1017/jfm.2012.166 Published online by Cambridge University Press

least in some parts of the domain as

$$\frac{\partial Q}{\partial s} = \text{constant} \times S^{\alpha/(\beta-1)}|Q|^{\beta/(\beta-1)} + \text{other terms}, \tag{A 9}$$

which hints at the possibility of Q blowing up at finite s. The offending term here is the dissipation term Ξ, which we have re-written as a function of S times $|Q|^{\beta/(\beta-1)}$. The physical issue is the positive feedback between increased flux and increased dissipation. However, in real glaciological settings, the finite size of the system generally prevents blow-up, and in all of the computations reported in this paper, the Picard iteration converged.

Appendix B. Water partitioning in the finite volume method

For a fixed ϕ, the one-dimensional mass conservation equation (3.19) must be solved wherever $\phi = \phi_m$ or $\phi = \phi_0$. With finite volume cells centred on the nodes of the mesh, and using upwind discretizations for the fluxes, (3.19) is advanced explicitly to determine the water volume in each cell:

$$V_{wi} = (Wh_{wi} + \tfrac{1}{2}S_{wi-} + \tfrac{1}{2}S_{wi+})\Delta x_i, \tag{B 1}$$

with Δx_i being the cell length, and $i\pm$ indicating the channel segments entering and leaving the cell. It is then a relatively simple matter of partitioning this available water between the channels and the sheet in that cell.

When $\phi = \phi_0$, $S_w = S$ is already known from step (g) in the solution procedure in § 3.7, so

$$S_{wi\pm} = S_{i\pm}, \quad h_{wi} = \left(V_{wi}/\Delta x_i - \tfrac{1}{2}S_{wi-} - \tfrac{1}{2}S_{wi+}\right)/W. \tag{B 2}$$

When $\phi = \phi_m$, h is already known from step (h) in the solution procedure, and either

$$S_{wi-} = S_{wi+} = 0, \quad h_{wi} = V_{wi}/\Delta x_i W \quad (\text{if this gives } h_{wi} \leqslant h_i), \tag{B 3a}$$

$$\text{or} \quad h_{wi} = h_i, \quad \tfrac{1}{2}S_{wi-} + \tfrac{1}{2}S_{wi+} = V_{wi}/\Delta x_i - Wh_i. \tag{B 3b}$$

This last possibility requires partitioning between the adjacent channels and there is nothing immediately to tell us how to do this. If we remember the neglected diffusive component $\rho_w g \mathscr{H}_w$ from ϕ_m, however, we conclude that an appropriate thing to do is to ensure that the water level is continuous between channels. Since the channels have known (and potentially different) areas $S_{i\pm}$, this is not necessarily the same as taking $S_{wi-} = S_{wi+}$; rather $\mathscr{H}_w(S_{wi-}, S_{i-}) = \mathscr{H}_w(S_{wi+}, S_{i+})$, where $\mathscr{H}_w(S_w, S)$ is the water depth in the channel. Assuming semicircular channels, this relationship is a little ungainly but can be written implicitly as

$$\tilde{S}_w(S, \mathscr{H}_w) := \frac{2S}{\pi}\sin^{-1}\left(\frac{\pi\mathscr{H}_w^2}{2S}\right)^{1/2} + \left(\frac{2S}{\pi}\right)^{1/2}\mathscr{H}_w\left(1 - \frac{\pi\mathscr{H}_w^2}{2S}\right)^{1/2}, \tag{B 4}$$

for the water-filled area $\tilde{S}_w$. Thus, (B 3b) can be written as

$$\tfrac{1}{2}\tilde{S}_w(S_{i-}, \mathscr{H}_{wi}) + \tfrac{1}{2}\tilde{S}_w(S_{i+}, \mathscr{H}_{wi}) = V_{wi}/\Delta x_i - Wh_i, \tag{B 5}$$

which can be solved to find $\mathscr{H}_{wi}$ and, hence, $S_{wi\pm}$. Note that employing this method at all of the underpressure nodes means that S_w is potentially different at either end of these channel segments. That is why we choose to define S_w on each end of the channels; but it should be noted that in the usual case, when $\phi > \phi_m$, we always have $S_w = S$ at both ends.

https://doi.org/10.1017/jfm.2012.166 Published online by Cambridge University Press

If, at the beginning of this procedure for $\phi = \phi_m$, the water-filled volume V_{wi} is actually larger than the total volume available in that cell,

$$V_i = (Wh_i + \tfrac{1}{2}S_{i-} + \tfrac{1}{2}S_{i+})\Delta x_i, \tag{B 6}$$

that node must become part of Ω^c at the next time step, and in order to conserve mass the excess water volume $V_{wi} - V_i$ is added to the neighbouring partially empty cell, effectively correcting the computed flux between those two cells.

Appendix C. Computation of steady states

In the one-dimensional steady state with constant positive input m, we write the total discharge as

$$\overline{Q} \equiv Q + Wq = k_c S_w^{\alpha} \psi^{\beta-1} + Wk h_w^{\alpha} \psi^{\beta-1}, \tag{C 1}$$

where $\psi = -\mathrm{d}\phi/\mathrm{d}x$ is always positive. The mass conservation equation (3.19) requires

$$\frac{\mathrm{d}\overline{Q}}{\mathrm{d}x} = Wm + \frac{\Xi}{\rho_w L}, \tag{C 2}$$

with the condition $\overline{Q} = \overline{Q}_N \equiv Q_N + Wq_N$ at $x = 0$. The general aim here is to integrate this equation, together with the ordinary differential equation for ϕ that is implicitly defined by (C 1), and for which the natural boundary condition is $\phi = \phi_m$ at the margin $x = x_m$. Since the dissipation term in (C 2) is small, we already have a good guess for $\overline{Q}$:

$$\overline{Q}(x) \approx \overline{Q}_N + \int_0^x Wm(x')\,\mathrm{d}x', \tag{C 3}$$

and since the boundary conditions are imposed on opposite ends we therefore propose to integrate backwards from the margin $x = x_m$, shooting for an initial value $\overline{Q}(x_m)$ in order to satisfy $\overline{Q} = \overline{Q}_N$ at $x = 0$. Some work is required before we can determine $\mathrm{d}\phi/\mathrm{d}x$ from (C 1), however.

For $\phi_m \leqslant \phi \leqslant \phi_0$, the steady sheet depth is always determined by the hydraulic potential, from (2.2):

$$h = \mathscr{H}(\phi) := \frac{u_b h_r}{u_b + l_r \tilde{A} |\phi_0 - \phi|^n}. \tag{C 4}$$

The steady-state channel area S, from (2.8), additionally depends on the dissipation term (3.22). Since $h_w = \mathscr{H}(\phi)$ unless $S_w = 0$ (in which case $h_w \leqslant \mathscr{H}(\phi)$), that can be written as

$$\Xi = [\overline{Q} - (1 - l_r/W)\min(Wk\mathscr{H}(\phi)^{\alpha}\psi^{\beta-1}, \overline{Q})]\psi. \tag{C 5}$$

(Note that the term in square brackets is the discharge carried in the channel and underlying sheet; unless the sheet is partially empty it is $\overline{Q} - (W - l_r)k\mathscr{H}(\phi)^{\alpha}\psi^{\beta-1}$.) The steady-state channel area from (2.8) can therefore be written in terms of hydraulic potential, discharge and potential gradient:

$$S = \mathscr{S}(\phi, \overline{Q}, \psi) := \frac{[\overline{Q} - (1 - l_r/W)\min(Wk\mathscr{H}(\phi)^{\alpha}\psi^{\beta-1}, \overline{Q})]\psi}{\rho_i L \hat{A} |\phi_0 - \phi|^n}. \tag{C 6}$$

Note that, unlike in the sheet-only case, it is not possible to have a steady state in which $\phi = \phi_0$, since S becomes arbitrarily large as ϕ_0 is approached (although we have

https://doi.org/10.1017/jfm.2012.166 Published online by Cambridge University Press

to allow this at the margins if $\phi_m = \phi_0$ there; additional physics could be added to prevent this but it is not a major concern of this paper (e.g. Evatt *et al.* 2006)).

When $\phi = \phi_m$, the sheet can only be partially filled ($h_w < h$) if the channel is empty ($S_w = 0$), so we can deduce from (C 1) that in that case:

$$h_w = \mathscr{H}_w(\overline{Q}) := \min\left(\left[\frac{\overline{Q}}{Wk\psi_m^{\beta-1}}\right]^{1/\alpha}, \mathscr{H}(\phi_m)\right), \tag{C 7}$$

and

$$S_w = \mathscr{S}_w(\overline{Q}) := \left[\max\left(\frac{\overline{Q} - Wk\mathscr{H}(\phi_m)^\alpha \psi_m^{\beta-1}}{k_C \psi_m^{\beta-1}}, 0\right)\right]^{1/\alpha}, \tag{C 8}$$

where $\psi_m = -\mathrm{d}\phi_m/\mathrm{d}x$.

When $\phi > \phi_m$, we have $h_w = h = \mathscr{H}$ from (C 4) and $S_w = S = \mathscr{S}$ from (C 6) and (C 1) therefore reads

$$\overline{Q} = k_c \mathscr{S}(\phi, \overline{Q}, \psi)^\alpha \psi^{\beta-1} + Wk\mathscr{H}(\phi)^\alpha \psi^{\beta-1}, \tag{C 9}$$

which implicitly determines $\psi = \Psi(\phi, \overline{Q})$. Assuming that this function is well defined, we have

$$\frac{\mathrm{d}\phi}{\mathrm{d}x} = \begin{cases} -\psi_m & \text{when } \phi = \phi_m \text{ and } \mathscr{S}_w(\overline{Q}) < \mathscr{S}(\phi, \overline{Q}, \psi_m) \\ \min(-\psi_m, -\Psi(\phi_m, \overline{Q})) & \text{when } \phi = \phi_m \text{ and } \mathscr{S}_w(\overline{Q}) = \mathscr{S}(\phi, \overline{Q}, \psi_m) \\ -\Psi(\phi, \overline{Q}) & \text{when } \phi_0 > \phi > \phi_m, \end{cases} \tag{C 10}$$

where, in the second case, the derivative is defined as x is approached from below. We can integrate (C 10) from $x = x_m$ to $x = 0$ together with (C 2), shooting to find the correct initial value for $\overline{Q}$. Once $\phi(x)$ has been found, it is a straightforward matter to define h, S, h_w and S_w from the appropriate combination of (C 4), (C 6), (C 7) and (C 8).

It is unfortunately not clear from (C 9) that there is only one solution for ψ, and hence whether $\Psi(\phi, \overline{Q})$ is a single-valued function. In fact, in general it is not; (C 9) can have one, two or three roots for ψ depending upon the various parameters. We interpret this as meaning that there is sometimes more than one possible steady state (see below). In many cases, however, $\Psi(\phi, \overline{Q})$ is well defined. In particular, it can be shown that if we only consider the sheet immediately below the channel, so $W = l_r$, then the steady state is always unique (the width l_r is supposed to represent roughly one cavity width, so the description as a 'sheet' in that case is unnecessary).

Multiple steady states arise when $W \gg l_r$, meaning that the sheet is very wide: the water can either be contained almost entirely in the sheet, in which case only a small portion of the total energy dissipated goes into heating the potential channel, or it can be localized in the channel with a much smaller proportion in the sheet. Typically, at low discharge only the first option is possible, and at high discharge only the second is possible; but there can occasionally be a region in between when either option gives rise to a viable steady state. This type of hysteresis for the steady states is essentially the same as found numerically in the two-dimensional network model of Schoof (2010). In fact for the one-dimensional case studied here, with uniform pressure required across the width of the sheet, multiple steady states are rather rare; they appear to be more common in the (presumably more realistic) two-dimensional model.

https://doi.org/10.1017/jfm.2012.166 Published online by Cambridge University Press

REFERENCES

BARTHOLOMEW, I., NIENOW, P., MAIR, D., HUBBARD, A., KING, M. A. & SOLE, A. 2010 Seasonal evolution of subglacial drainage and acceleration in a Greenland outlet glacier. *Nat. Geosci.* **3**, 408–411.

BINDSCHADLER, R. 1983 The importance of pressurized subglacial water in separation and sliding at the glacier bed. *J. Glaciol.* **28**, 239–265.

BUDD, W. F., KEAGE, P. L. & BLUNDY, N. A. 1979 Empirical studies of ice sliding. *J. Glaciol.* **23**, 157–170.

COPLAND, L., SHARP, M. J. & NIENOW, P. W. 2003 Links between short-term velocity variations and the subglacial hydrology of a predominantly cold polythermal glacier. *J. Glaciol.* **49**, 337–348.

CREYTS, T. T. & SCHOOF, C. 2009 Drainage through subglacial water sheets. *J. Geophys. Res.* **114**, F04008.

EKELAND, I. & TEMAM, R. 1976 *Convex Analysis and Variational Problems*. North-Holland.

EVATT, G. W., FOWLER, A. C., CLARK, C. D. & HULTON, N. R. J. 2006 Subglacial floods beneath ice sheets. *Phil. Trans. R. Soc.* A **364**, 1769–1794.

FLOWERS, G., CLARKE, G. K. C., BJÖRNSSON, H. & PÁLSSON, F. 2004 A coupled sheet-conduit mechanism for Jökulhlaup propagation. *Geophy. Res. Lett.* **31**.

FLOWERS, G. E. & CLARKE, G. K. C. 2002 A multicomponent coupled model of glacier hydrology 1. Theory and synthetic examples. *J. Geophys. Res.* **107**.

FOUNTAIN, A. G. & WALDER, J. S. 1998 Water flow through temperate glaciers. *Rev. Geophys.* **36**, 299–328.

FOWLER, A. C. 1986 A sliding law for glaciers of constant viscosity in the presence of subglacial cavitation. *Proc. R. Soc. Lond.* A **407**, 147–170.

FOWLER, A. C. 1987 A theory of glacier surges. *J. Geophys. Res.* **92**, 9111–9120.

GLOWINSKI, R. 1984 *Numerical Methods for Nonlinear Variational Problems*. Springer.

GORDON, S., SHARP, M., HUBBARD, B., SMART, C., KETTERLING, B. & WILLIS, I. 1998 Seasonal reorganization of subglacial drainage inferred from measurements in boreholes. *Hydrol. Process.* **12**, 105–133.

HEWITT, I. J. 2011 Modelling distributed and channelized subglacial drainage: the spacing of channels. *J. Glaciol.* **57**, 302–314.

HEWITT, I. J. & FOWLER, A. C. 2008 Seasonal waves on glaciers. *Hydrol. Process.* **22**, 3919–3930.

HOCK, R. & HOOKE, R. LEB 1993 Evolution of the internal drainage system in the lower part of the ablation area of Storglaciären, Sweden. *Geol. Soc. Am. Bull.* **105**, 537–546.

HOOKE, R. LEB., BRZOZOWSKI, J. & BRONGE, C. 1983 Seasonal variations in surface velocity, Storglaciären, Sweden. *Geografis. Annal.* **65**, 263–277.

IKEN, A. & BINDSCHADLER, R. A. 1986 Combined measurements of subglacial water pressure and surface velocity of Findelengletscher, Switzerland: conclusions about drainage system and sliding mechanism. *J. Glaciol.* **32**, 101–119.

JANSSON, P. 1996 Dynamics and hydrology of a small polythermal valley glacier. *Geografis. Annal.* **78**, 171–180.

JOUGHIN, I., DAS, S. B., KING, M. A., SMITH, B. E., HOWAT, I. M. & MOON, T. 2008 Seasonal speedup along the Western flank of the Greenland ice sheet. *Science* **320**, 781–783.

KAMB, B. 1987 Glacier surge mechanism based on linked cavity configuration of the basal water system. *J. Geophys. Res.* **92**, 9083–9100.

KAMB, B., RAYMOND, W. D., HARRISON, W. D., ENGELHARDT, H., ECHELMEYER, K. A., HUMPHREY, N., BRUGMAN, M. M. & PFEFFER, T. 1985 Glacier surge mechanism: 1982–1983 surge of Variegated Glacier, Alaska. *Science* **227**, 469–479.

LEVEQUE, R. 2002 *Finite Volume Methods for Hyperbolic Equaions*. Cambridge University Press.

LLIBOUTRY, L. 1969 Contribution à la théorie des ondes glaciaires. *Can. J. Earth Sci.* **6**, 943–953.

NIENOW, P., SHARP, M. & WILLIS, I. 1998 Seasonal changes in the morphology of the subglacial drainage system, Haut Glacier d'Arolla, Switzerland. *Earth Surf. Process. Landforms* **23**, 825–843.

https://doi.org/10.1017/jfm.2012.166 Published online by Cambridge University Press

NYE, J. F. 1976 Water flow in glaciers: Jökulhlaups, tunnels and veins. *J. Glaciol.* **17**, 181–207.

PATERSON, W. S. B. 1994 *The Physics of Glaciers*. Butterworth-Heinemann.

PIMENTEL, S. & FLOWERS, G. E. 2010 A numerical study of hydrologically driven glacier dynamics and subglacial flooding. *Proc. R. Soc.* A **467**, 537–558.

RAYMOND, C. F., BENEDICT, R. J., HARRISON, W. D., ECHELMEYER, K. A. & STURM, M. 1995 Hydrological discharges and motion of Fels and Black Rapids Glaciers, Alaska, USA: implications for the structure of their drainage systems. *J. Glaciol.* **41**, 290–304.

RÖTHLISBERGER, H. 1972 Water pressure in intra- and subglacial channels. *J. Glaciol.* **11**, 177–203.

SCHOOF, C. 2005 The effect of cavitation on glacier sliding. *Proc. R. Soc. Lond.* A **461**, 609–627.

SCHOOF, C. 2010 Ice-sheet acceleration driven by melt supply variability. *Nature* **468**, 803–806.

SCHOOF, C., HEWITT, I. J. & WERDER, M. A. 2012 Flotation and open water flow in a model for subglacial drainage. Part 1. Distributed drainage. *J. Fluid Mech.* **702**, 126–156.

SCHULER, T. V. & FISCHER, U. H. 2009 Modelling the diurnal variation of tracer transit velocity through a subglacial channel. *J. Geophys. Res.* **114**.

SHEPHERD, A., HUBBARD, A., NIENOW, P., KING, M., MCMILLAN, M. & JOUGHIN, I. 2009 Greenland ice sheet motion coupled with daily melting in late summer. *Geophys. Res. Lett.* **36**.

SHREVE, R. L. 1972 Movement of water in glaciers. *J. Glaciol.* **11**, 205–214.

SPRING, U. & HUTTER, K. 1982 Conduit flow of a fluid through its solid phase and its application to intraglacial channel flow. *Intl J. Engng Sci.* **20**, 327–363.

TSAI, V. C. & RICE, J. R. 2010 A model for turbulent hydraulic fracture and application to crack propagation at glacier beds. *J. Geophys. Res.* **115**.

VAN DE WAL, R. S. W., BOOT, W., VAN DEN BROEKE, M. R., SMEETS, C. J. P. P, REIJMER, C. H., DONKER, J. J. A. & OERLEMANS, J. 2008 Large and rapid melt-induced velocity changes in the ablation zone of the Greenland ice sheet. *Science* **321**, 111–113.

WALDER, J. S. 1986 Hydraulics of subglacial cavities. *J. Glaciol.* **32**, 439–445.

WALDER, J. S. & FOWLER, A. C. 1994 Channelized subglacial drainage over a deformable bed. *J. Glaciol.* **40**, 3–15.

WILLIS, I. C. 1995 Interannual variations in glacier motion - a review. *Prog. Phys. Geog.* **19**, 61–106.

ZWALLY, H. J., ABDALATI, W., HERRING, T., LARSON, K, SABA, J. & STEFFEN, K. 2002 Surface melt-induced acceleration of Greenland ice-sheet flow. *Science* **297**, 218–222.

https://doi.org/10.1017/jfm.2012.166 Published online by Cambridge University Press